A High-Precision Sub-Grid Parameterization Scheme for Clear-Sky Direct Solar Radiation in Complex Terrain in the Atmospheric Model

Changyi Li[1] ID, **Wei Wu**[1] ID, **Yanan Chen**[1] ID, **Guili Feng**[1] ID, **Xiaopei Wen**[1]

[1] Shandong Institute of Meteorological Sciences, Jinan, China

Corresponding author: Wei Wu (wuwei_sd@163.com)

Key Points:

- For clear-sky direct solar radiation in terrain, the most accurate geometric model so far and a parameterized correction term are proposed
- Eleven reduced calculation methods and 2–3 order finite difference slope algorithms can no longer be used because errors
- Overall improvements constitute a high-precision sub-grid parameterization scheme for clear-sky direct solar radiation in complex terrain

Abstract

Research shows that complex terrain can affect the spatial distribution of solar radiation and atmospheric physical processes. Based on the high-resolution topographic data, there are already several parameterization schemes available to couple the terrain effects on solar radiation with atmospheric models. However, to reduce the amount of calculation, some methods that can lead to errors are used in the sub-grid parameterization schemes for clear-sky direct solar radiation (SPS-CSDSR). In addition, the common finite difference slope algorithms and the assumption of consistent sub-grid atmospheric transparency can also result in errors. This renders existing SPS-CSDSRs unsuitable for complex terrain in middle and high latitudes and in turbid weather. In this study, these three problems have been effectively solved. The most accurate geometric algorithms for direct solar radiation so far, a

high-precision and fast terrain occlusion algorithm and the triangulated sub-grid algorithm, are proposed. On Taiwan Island, the accuracy of the two methods is verified in the virtual vacuum atmosphere. Based on the fact that atmospheric transparency actually increases with altitude, a correction term based on sub-grid anomaly altitude is proposed for converting the sub-grid terrain effect factors into the atmospheric model. Overall improvements constitute a high-precision SPS-CSDSR in complex terrain. Eleven reduced calculation methods and common finite difference slope algorithms can no longer be used. In further study, atmospheric models need improvement in coupling the terrain effects on solar radiation to accurately describe vertical distributions. In this case, the high-precision scheme proposed in this study can play a key role.

Plain Language Summary

Research shows that complex terrain can affect the spatial distribution of solar radiation and atmospheric physical processes. Based on the high-resolution topographic data, there are already several parameterization schemes available to couple the terrain effects on solar radiation with atmospheric models. However, to reduce the amount of calculation, some methods that can lead to errors are used in the sub-grid parameterization schemes for clear-sky direct solar radiation. In this study, problems on errors have been effectively solved. The most accurate geometric algorithms for direct solar radiation so far, a high-precision and fast terrain occlusion algorithm and the triangulated sub-grid algorithm, are proposed. Based on the fact that atmospheric transparency actually increases with altitude, a correction term based on sub-grid anomaly altitude is proposed for converting the sub-grid terrain effect factors into the atmospheric model. Overall improvements constitute a high-precision parameterization scheme for clear-sky direct solar radiation in complex terrain. Eleven reduced calculation methods and common finite difference slope algorithms can no longer be used. In further study, atmospheric models need improvement in coupling the terrain effects on solar radiation to accurately describe vertical distributions. In this case, the high-precision scheme proposed in this study can play a key role.

1. Introduction

The spatial distribution of clear-sky solar irradiance can be strongly affected by terrain factors (altitude, slope, slope direction, and terrain occlusion, etc) (Swift, 1976; Dubayah & Rich, 1995; Kumar et al. 1997; Fu, 2000; Hofierka & Suri, 2002). Converting the clear-sky solar irradiance in complex terrain based on high-resolution DEM (Digital Elevation Model) data to atmospheric models with several to 100 kilometers of horizontal resolution, which will also be significantly different from that on the flat (Zhang et al., 2006; Essery & Marks, 2007; He at al., 2019; Huang et al., 2022). In order to introduce the terrain effects on solar radiation into the atmospheric model, sub-grid parameterization schemes based on high-resolution DEM data are developed to couple terrain effects on direct solar radiation, diffuse radiation, and reflected radiation with atmospheric model variables (Dubayah et al., 1990; Essery & Marks, 2007; Gu et al., 2020; He et al., 2019; Helbig & Löwe, 2012; Huang et al., 2022; Müller & Scherer, 2005; Zhang et al., 2006; Zhang et al., 2022). The coupling simulation experiments show that terrain effects on solar radiation can change the simulation results of the energy budget, surface temperature, and precipitation, such as in the Tibetan Plateau and related regions (Cai et al., 2023; Gu et al., 2020; Gu et al., 2022; Hao et al., 2021; Müller & Scherer, 2005; Yue et al., 2021; Zhang et al., 2006; Zhang et al., 2022). In order to reduce the computational cost, many methods that may lead to significant errors are employed in SPS-CSDSR for complex terrain.

The power of direct solar radiation received in complex terrain can be measured by the clear-sky horizontal direct solar irradiance (CSHDSI), which represents the total direct solar radiation received per unit area of a horizontal plane per unit time. The CSHDSI in an atmospheric model grid cell can be calculated from which in sub-grid cells by the following equations:

$$CSHDSI_{mt} = \frac{1}{N_s}\sum_{k=1}^{N_s} CSHDSI_{sk} \tag{1}$$

with

$$\begin{cases} CSHDSI_{sk} = DNI_{sk} \cdot MAX(cos\theta_{sk}, 0.0) \cdot SF_{sk} \cdot A_{sk}/A_{shk} & (2) \\ cos\,\theta_{sk} = cos\,\beta_{sk}\,sin\,\alpha_{sk} + sin\,\beta_{sk}\,cos\,\alpha_{sk}\,cos(\varphi_{sk} - \gamma_{sk}). & (3) \end{cases}$$

Where $m, t, s,$ and h indicate the atmospheric model grid cell, terrain, sub-grid cell, and horizontal plane. N_s and k are the number of sub-grid cells within an atmospheric model grid cell and the sequence number of a sub-grid cell, respectively. DNI is the Direct Normal Irradiance. In the sub-grid cell k, θ_{sk} is the angle between the plane normal and the solar beam, SF_{sk} is the shading factor (0 for shadow, 1 for shadowless). A_{sk} and A_{shk} are the surface area and horizontal plane area of the sub-grid cell, respectively. Equation 3 is given by Kondratyev (1977), in which θ_{sk} depends on slope β_{sk}, aspect (slope direction) γ_{sk} (0 for the north, and increasing clockwise), solar altitude angle α_{sk} between the solar beam and the horizontal plane, and solar azimuth angle φ_{sk}.

The existing SPS-CSDSRs use the basic assumption that a sub-grid cell and its parent grid cell have the same DNI, i.e., $DNI_{sk} \approx DNI_m$, thus establishing

$$CSHDSI_{mtp} \approx DNI_m \cdot f_{mtp} \tag{4}$$

with

$$f_{mtp} = \frac{1}{N_s}\sum_{k=1}^{N_s}(MAX(cos\theta_{sk}, 0.0) \cdot SF_{sk} \cdot A_{sk}/A_{shk}), \tag{5}$$

where p indicates parameterization. DNI_m can be obtained from the radiation model of atmospheric model. The f_{mtp} depends only on the solar position and terrain factors, which can be calculated offline earlier than the atmospheric model runs. Equations 4–5 are other forms in some SPS-CSDSRs.

Because calculating terrain occlusion requires evaluating each point in the solar direction, the calculation for f_{mtp} based on high-resolution DEM data is quite intensive. The early computers had slow calculation speeds, and there was a lack of a high-precision and fast terrain occlusion algorithm. As a result, numerous methods have been proposed to reduce calculations (Table 1). Due to the lack of precise models for comparison and the difficulty of observational verification, the accuracy of these methods has not been fully confirmed in complex terrain.

126 **Table 1**. The methods to reduce calculation for f_{mtp} in complex terrain.

Index	Method	User	Our views on using them
1	Ignoring shadows.	Dubayah (1990); He (2019), Gu (2020); Zhang (2006).	The $CSHDSI_{mt}$ will be significantly overestimated.
2	Assuming that sub-grid cells in a atmospheric model grid cell have the same slope and the slope direction is evenly distributed in all directions.	Dubayah (1990).	It does not apply to the areas where the model grid cell has many hills. Especially when vertical distribution needs to be taken seriously.
3	Using low resolution DEM data.	Muller & Scherer (2005) used the 30" (~1 km); Zhang (2006) used the 5' (~9 km).	Underestimating terrain effect.
4	Using a function to predict the fraction of the surface in shadow in the atmospheric model grid.	Essery & Marks (2007).	It lacks of proof of universal applicability.
5	Ignoring A_{sk}/A_{shk}.	He (2019); Gu (2020), Zhang (2022).	The $CSHDSI_{mt}$ will be seriously underestimated.
6	Using average terrain factors in the atmospheric model grid, such as the slope cosine $cos\,\beta_m = \frac{1}{N_s}\sum_{k=1}^{N_s} cos\theta_{sk}$.	He (2019); Zhang (2022), Huang (2022).	This results in the need to use the shadowless coverage factor. If the shadows are not evenly distributed with the size of $CSHDSI_{sk}$, it will lead to errors.
7	*Using shadowless coverage factor $SFC_m = \frac{1}{N_s}\sum_{k=1}^{N_s} SF_{sk}$.	Zhang (2022).	Shadows often occur in the low $cos\theta_{sk}$ regions. This will underestimate $CSHDSI_{mt}$.
8	** Correcting SFC_m to SFC_p by a function of model horizontal resolution (km) to reduce excessive shadows.	Huang (2022).	There is no clear physical relationship between the atmospheric model horizontal resolution and SFC_m. It is not applicable on non-uniform shadows.
9	Using small radius for searching occlusion.	Huang (2022) used the 27 km; Zhang (2022) used the 9 km; and others are unknown or ignoring shadows.	The $CSHDSI_{mt}$ will be overestimated.
10	Ignoring the earth's curvature.	Usually it is.	At low solar altitude angles, the $CSHDSI_{mt}$ will be underestimated.
11	Ignoring that mountains can get sunlight when the solar altitude angle is below zero.	Usually it is.	The $CSHDSI_{mt}$ in mountains may be underestimated.

127 * $f_{mtp} = SFC_m \cdot f_{other}$, f_{other} will be calculated in another way. ** $SFC_p = 1 - C_{ad}(1 - SFC_m)$ with $C_{ad} =$
128 $0.1849dx^{-1.443} + 0.04561$. dx is the atmospheric model horizontal resolution (km).
129
130 In addition, the slope algorithms may also affect the accuracy of the CSHDSI calculation.
131 Tang et al. (2013) found statistical differences in slope results across 8 algorithms. Four
132 scholars believe that the slope accuracy of the third-order finite difference algorithm (3FDA)

is higher than that of the second-order finite difference algorithm (2FDA), while three scholars have reached the opposite conclusion (Liu et al., 2004). Using 10-meter-resolution DEM data of a concave ellipsoid surface and a Gauss-synthesized surface, Liu et al. (2004) point out that 2FDA has the highest accuracy under high-quality DEM data, while 3FDA has the highest accuracy under low-quality DEM data.

Up to now, the effect of slope finite difference algorithms on the accuracy of calculating CSHDSI has not received any attention. 2FDA and 3FDA algorithms are commonly used. For example, Dozier & Frew (1990), Dubayah et al. (1990) used 2FDA, and Huang et al. (2022) used 3FDA.

The actual atmospheric transparency usually increases with altitude, as does DNI. The existing SPS-CSDSRs are all based on the assumption that a sub-grid cell and its parent grid cell have the same DNI, which may result in deviation.

Usually, direct solar radiation occupies the highest proportion during clear skies in the daytime, especially in the mountains. It can be used as a parameterized factor for diffuse radiation and reflected radiation. Therefore, ensuring the accuracy of the calculation for direct solar radiation is crucial. The purpose of this study is to optimize algorithms and schemes in order to reduce reliance on reduced calculation methods, and enhance the accuracy of SPS-CSDSR in complex terrain.

2. Three Improvements

2.1 Triangulating the Sub-grid

The smooth effects of 2FDA and 3FDA can cause errors in calculating CSHDSI in sub-grid cells (The analysis result is presented in Chapter 4.1 of this paper). As a result, the tow triangular planes algorithm (2TPA) has been developed.

In Figure 1, (i, j) represent the grid coordinates of the DEM data. The two triangles are formed by connecting coordinate points. When $tan\,\varphi_{sk} \geq 0$, the triangles in a sub-grid cell are positioned in the northwest and southeast. When $tan\,\varphi_{sk} < 0$, they are positioned in the

northeast and southwest. This can reduce the occlusion of adjacent grid lines. α_{sk}, φ_{sk}, and SF_{sk} will be calculated at the center (i', j') of the DEM grid cell. The grid lines closest to (i', j') are not included in the occlusion calculation; otherwise, there are too many shadows when using the 90-meter horizontal resolution DEM data (DEM90). The "Local Altitude" H_A of (i', j') is the average of altitudes at four coordinate points surrounding it, and this, altitude will be used except for calculating occlusion.

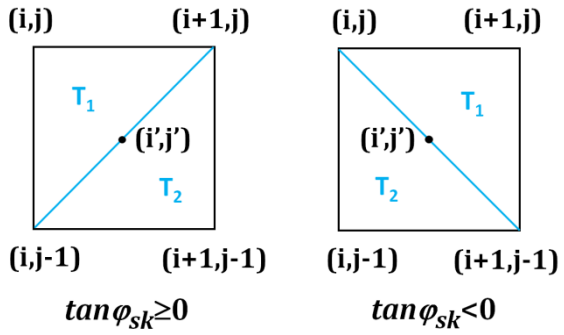

Figure 1. The Schematic diagram of the two triangles algorithm for CHSDSI. (i, j) represents the grid coordinates of the DEM data. The point (i', j') at the center.

Based on Equation 1, the equation to calculate $CSHDSI_{mt}$ from its triangulated sub-grid CHSDSI is:

$$CSHDSI_{mt} = \frac{1}{N_s}\sum_{k=1}^{N_s} DNI_{sk} \cdot SF_{sk} \cdot TCS_{sk} \quad (6)$$

with

$$TCS_{sk} = \sum_{g=1}^{2}(MAX(cos\theta_{skg}, 0.0) \cdot A_{skg}/A_{shk}), \quad (7)$$

where g is a triangular serial number, θ_{skg} is the angle between the normal of the triangular plane and the solar beam, and A_{skg} is the triangle area calculated using Heron's formula. TCS_{sk} is a composition-factor of the tow triangles in sub-grid cell.

The slope β_{sk} and aspect γ_{sk} of the sub-grid are calculated by the following equations (Li and Weng, 1987):

$$\beta_{sk} = arctan\sqrt{\left(\frac{\partial H}{\partial x}\right)^2 + \left(\frac{\partial H}{\partial y}\right)^2}. \quad (8)$$

$$\gamma_{sk} = \begin{cases} \frac{3\pi}{2} - arctan\left(\frac{\partial H}{\partial y} / \frac{\partial H}{\partial x}\right), i \quad \frac{\partial H}{\partial x} > 0 \\ \frac{\pi}{2} - arctan\left(\frac{\partial H}{\partial y} / \frac{\partial H}{\partial x}\right), if \ \frac{\partial H}{\partial x} < 0 \\ 0, if \ \frac{\partial H}{\partial x} = 0 \ \ \frac{\partial H}{\partial y} < 0 \\ \pi, if \ \frac{\partial H}{\partial x} = 0 \ \ \frac{\partial H}{\partial y} > 0 \\ undefined, if \ \frac{\partial H}{\partial x} = 0 \ \ \frac{\partial H}{\partial y} = 0 \end{cases} . \quad (9)$$

$\frac{\partial H}{\partial x}$ and $\frac{\partial H}{\partial y}$ are calculated by coordinates and altitudes at the three points of triangle. For example, when $tan\,\varphi_{sk} < 0$, in triangle T_2,

$$\begin{cases} \frac{\partial H}{\partial x} = (H_{i+1,j-1} - H_{i,j-1})/D_x \\ \frac{\partial H}{\partial y} = (H_{i,j} - H_{i,j-1})/D_y \end{cases}, \quad (10)$$

where D_x and D_y are the east-west and north-south spacing of the DEM data, respectively.

2FDA and 3FDA will be examined in Chapter 4.1, whose equations are as follows:

2FDA (Dozier & Frew, 1990)

$$\begin{cases} \frac{\partial H}{\partial x} = (H_{i+1,j} - H_{i-1,j})/(2 \cdot D_x) \\ \frac{\partial H}{\partial y} = (H_{i,j+1} - H_{i,j-1})/(2 \cdot D_y) \end{cases}. \quad (11)$$

3FDA (Sharpnack & Akin, 1969)

$$\begin{cases} \frac{\partial H}{\partial x} = (H_{i+1,j+1} - H_{i-1,j+1} + H_{i+1,j} - H_{i-1,j} + H_{i+1,j-1} - H_{i-1,j-1})/(6 \cdot D_x) \\ \frac{\partial H}{\partial y} = (H_{i-1,j+1} - H_{i-1,j-1} + H_{i,j+1} - H_{i,j-1} + H_{i+1,j+1} - H_{i+1,j-1})/(6 \cdot D_y) \end{cases}. \quad (12)$$

When using 2FDA and 3FDA for calculating CSHDSI, the equation $A_{sk}/A_{shk} = 1/cos\,\beta_{sk}$ will be used together in Equations 2 and 5.

2.2 The High-Precision and Fast Terrain Occlusion Algorithm (HPFTOA)

The HPFTOA uses a dynamic lossless search occlusion radius to expedite calculations while also considering the earth's curvature. The most methods in Table 1 are aimed at reducing the calculations associated with terrain occlusion. Therefore, the detailed algorithm with high

precision and fast speed is given here. This algorithm cannot be implemented in an interpreted programming language such as Python. Fortran 90 was used in this study.

There are five steps to determine whether point A is obscured in Figure 2.

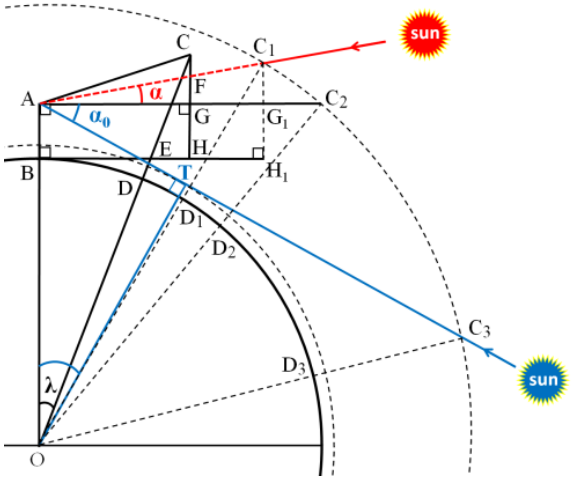

Figure 2. Terrain occlusion calculation and analysis diagram. The point O is the center of the earth.

2.2.1 Determining Whether Point A is Obscured by the Horizon in the Data Area

The area of CSHDSI is defined as the study area, while the area of used data is defined as the data area. The calculation for occlusion requires that the data area be larger than the study area. The method for determining the size of the data area is given in 2.2.2.

Firstly, the lowest solar altitude angle α_0 in the study area is calculated. When the solar altitude angle $\alpha \leq \alpha_0$, point A is obscured by the horizon with an altitude H_{min0}. H_{min0} is the minimum altitude in the data area.

In Figure 2, the point O is the center of the earth, the line AG is horizontal, and the line AT is the tangent of the sphere with a radius $(R_0 + H_{min0})$. T, R_0, and H_A are the tangent point, the earth's radius, and the altitude of point A. According to geometry, the angle α_0 equals the angle AOT, then

$$\alpha_0 = -arccos((R_0 + H_{min0})/(R_0 + H_A)). \quad (13)$$

The study area can be divided into many small rectangular regions to quickly determine whether these regions are completely obscured by the horizon. A smaller search occlusion radius in the small data area can also be obtained.

2.2.2 Obtaining the Maximum Search Occlusion Radius in the Data Area

The idea is to take the farthest distance, where the highest point in the data area can occlude point A, as the maximum search occlusion radius ($SRA_{\max}$). Set H_{max0} represents the maximum altitude in the data area. In Figure 2, the altitudes of points C_1,C_2,and C_3 are H_{max0}. The line AC_2 is horizontal. The points B, D_1,D_2, and D_3 are the sea level coordinate positions of points A, C_1, C_2, and C_3. Similar to the principle of analyzing radar terrain masking (Zhou et al., 2013) (The analysis is omitted here.), the equation for SRA_{max} is as follows:

$$SRA_{max} = \begin{cases} min(R_1, R_2), if\ \alpha \geq 0 \\ R_3 + R_4, if\ \ \alpha_0 < \alpha < 0 \end{cases} \tag{14}$$

with

$$\begin{cases} R_1 = (H_{max0} - H_A) / tan\,\alpha_s \\ R_2 = \sqrt{(H_{max0} - H_A)(2R_0 + H_{max0} + H_A)} \\ R_3 = \sqrt{(H_A - H_{min0})(2R_0 + H_A + H_{min0})} \\ R_4 = \sqrt{(H_{max0} - H_{min0})(2R_0 + H_{max0} + H_{min0})} \end{cases}.$$

This study adopts the simplification as shown in $R_2 = \sqrt{2(H_{max0} - H_A)(R_0 + H_{max0})}$ to speed up.

When $\alpha < 0$, the width of the data area increases by $2R_4$ around the study area to calculate occlusion. When $\alpha \geq 0$, the width is R_4.

2.2.3 Determining Whether Point A is Obscured by the Horizon in Solar Azimuth

First, in the solar azimuth, a set of altitudes H_c of point C is obtained from DEM data within SRA_{max}. That is the same principle used in 2.2.1 to determine whether point A is obscured by the horizon with an altitude H_{min}. H_{min} is the minimum value of H_c.

To obtain H_c:

(1) For latitude-longitude grid, the grid coordinates (including decimals) of H_c are the intersections of the lines with the solar azimuth angle and the rectangular grid. When determining whether point C obscures point A, H_c is the linear interpolation of altitudes of two nearby DEM data points. For other cases, the grid coordinates of H_c can be converted to integers to speed up the calculation. This method has been verified.

Due to the curvature of the latitude line, there is an error in the coordinate of C. When the error exceeds half of the DEM data spacing, the 2.2.3(2) algorithm is used. At this time, the distance between the coordinates of A and C is defined as LC_{grid}.

In the actual calculation, a lookup table algorithm is used to obtain LC_{grid}, and the calculation for coordinates of C by the rectangular grid is within LC_{grid}. The lookup table, based on the DEM data spacing and latitude, has to be calculated in advance.

When using 2TPA, the calculation for coordinates of point C does not include the grid lines closest to the local point (i', j') in Figure 1. For the usual case where the local point (i, j) corresponds to the coordinate position of the DEM data, the grid lines closest to (i, j) should be included. This is related to the spacing of DEM data. The spacing here is 90 meter.

The following method is used to reduce the calculation time: if $|\sin\varphi_{sk}| \geq 0.5$, select the longitude lines to calculate the intersections; if $|\sin\varphi_{sk}| \leq 0.8$, select the latitude lines.

(2) If the search distance $Lc > LC_{grid}$, the latitude-longitude coordinates of point C are calculated using Equation 15 with the solar azimuth φ_{sk} and Lc. Then the coordinates are converted to grid coordinates as integers (Pay attention to the negative longitude.). Equation

15 is from Aviation Formulary V1.47 (Ed., 2013). For speeding up, it is simplified based on that the $SRA_{\max}$ being less than 700 km for Mount Everest and sea level.

$$\begin{cases} d = Lc/R_0 \\ tc = 2\pi - \varphi_{sk} \\ latC = arcsin(sin(latA)\,cos(d) + cos(latA) \cdot d \cdot cos(tc)) \\ lonC = \begin{cases} lonA, if\ \cos(latA) = 0 \\ mod((lonA - arcsin(sin(tc) \cdot d/cos(latC)) + \pi, 2\pi) - \pi, if\ \cos(latA) \neq 0 \end{cases} \end{cases} . \quad (15)$$

Where $lonA$ and $latA$ are the latitude and longitude of point A. Lc is determined by incrementally increasing the value of D_{LC} on LC_{grid}. The D_{LC} can be 1–3 times as much as D_y. This depends on the balance between the accuracy and speed of calculation.

For the latitude-longitude grid, a smaller LC_{grid} at high latitudes results in slower calculation speed. The appropriate map projection can be selected to reduce calculation time.

2.2.4 Obtaining the Search Occlusion Radius in Solar Azimuth

In the same principle as 2.2.2, the search occlusion radius SRS_{max} in solar azimuth can be obtained based on H_c.

2.2.5 Determining Whether A is Obscured Within SRS_{max}

In Figure 2, the points B and D are the coordinates of points A and C at sea level. The lines AG and BH are horizontal. The lines AB and CH are perpendicular to the lines AG and BH. The point F is the intersection of the solar ray and the line CH. λ is the angle AOC. H_A and H_c are the altitudes of points A and C, respectively. α_s is the solar altitude angle.

The H_{GC} (line GC) is compared with the H_{GF} (line GF) to determine whether point A is obscured, as in Equation 16. L_{BD} is the arc distance between points B and D.

$$SF_{sk} = \begin{cases} 0, H_{GC} \geq H_{GF} \\ 1, H_{GC} < H_{GF} \end{cases} \quad (16)$$

with

$$\begin{cases} \lambda = L_{BD}/R_0 \\ L_{DE} = R_0/cos\,\lambda - R_0 \\ H_{GC} = (H_c - L_{DE}) \cdot cos\,\lambda - H_A \\ H_{GF} = (R_0\,tan\,\lambda + (H_c - L_{DE})\,sin\,\lambda)) \cdot tan\,\alpha_s \end{cases} .$$

Because considering the earth's curvature, Equation 16 is also applicable when the solar altitude angle $\alpha < 0$. The analysis diagram is omitted.

2.3 Add a Sub-grid Altitude Anomaly Correction Term to Parameterization

As the actual atmospheric transparency increases with altitude, so does DNI. The existing SPS-CSDSRs are all based on the assumption that a sub-grid cell and its parent grid cell have the same DNI, which may lead to errors.

The DNI model (Equation 17) from the Solar Radiation Model *r.sun* will be used to observe the changes in DNI with altitude.

$$DNI_{sk} = G_0 exp(-0.8662 T_{LK} m \delta(m)) \quad (17)$$

with

$$\begin{cases} G_0 = I_0\left(1.0 + 0.03344 \cdot cos(2\pi N_d/365.25 - 0.048869)\right) & (18) \\ m = exp\,(-H/8434.5)/(sin\alpha + 0.50572(\alpha + 6.07995)^{-1.6364}) & (19) \\ \dfrac{1}{\delta(m)} = \begin{cases} 6.6296 + 1.7513m - 0.1202m^2 + 0.0065m^3 - 0.00013m^4, & if\ m \le 20 \\ 10.4 + 0.718m, & if\ m > 20 \end{cases} & (20) \end{cases} .$$

Where G_0 is the extra-terrestrial irradiance, $I_0 = 1367 \mathrm{W/m^2}$ (the solar constant), N_d is the day number starting from 1th January of the year, T_{LK} is the Linke turbidity factor for an air mass equal to 2, H is the altitude, and α is the solar altitude angle (in degrees).

The *r.sun* can calculate direct, diffuse, reflective, and total solar irradiance (Hofierka & Suri, 2002). It has been implemented in the GRASS® Geographic Information System environment (Neteler & Mitasova, 2008), and its applicability has been demonstrated by the works of Hofierka & Kaňuk (2009), Nguyen & Pearce (2010), Pintor et al. (2015), and Ruiz-Arias et al. (2009).

Equation 17 is from the model of direct solar radiation in the *r.sun*. Like the atmospheric model, Equation 17 does not take into account atmospheric refraction. According to Hofierka & Suri (2002), Equation 17 is from Rigollier et al. (2000). Equations 18 and 19 are from Kasten & Young (1989) and Kasten (1996), severally.

Equation 21 is used to simulate T_{LK} changes with altitude, which borrows from Remund (2003). T_{LK0} is the T_{LK} at zero altitude.

$$T_{LK} = exp(ln(T_{LK0})(1 - H/(2 \cdot 8435)). \quad (21)$$

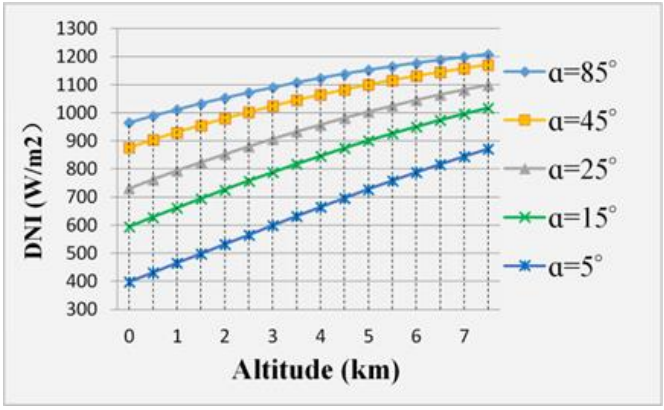

Figure 3. The curves of DNI with altitude when taking $T_{LK0} = 3.0$ in Equation 17. α is the solar altitude angle..

Taking $T_{LK0} = 3.0$ in Equation 17, a set of curves showing DNI with altitude at different solar altitude angles is obtained (Figure 3). Upon observing Figure 3, it is evident that DNI increases in an approximately linear fashion with altitude. In an atmospheric model grid cell, assuming that the DNIs in the horizontal direction are same, then

$$DNI_{sk} \approx DNI_m + RDNI_{Hm} \cdot (H_{sk} - H_m). \quad (22)$$

Where DNI_m is in the atmospheric model grid, and $RDNI_{Hm}$ is the vertical change rate of DNI_m. Then Equation 6 is changed to

$$CSHDSI_{mtp} \approx DNI_m \cdot f_{mtp} + \Delta CSHDSI_{mtph} \quad (23)$$

with

$$\begin{cases} f_{sk} = SF_{sk} \sum_{g=1}^{2} (MAX(cos\theta_{skg}, 0.0) \cdot A_{skg}/A_{shk}) \\ f_{mtp} = \frac{1}{N_s} \sum_{k=1}^{N_s} f_{sk} \\ \Delta CSHDSI_{mtph} = RDNI_{Hm} \frac{1}{N_s} \sum_{k=1}^{N_s} (H_{sk} - H_m) \cdot f_{sk} \end{cases} . \quad (24)$$

Equation 23 has one more term $\Delta CSHDSI_{mtph}$ than Equation 4. Usually, H_m is the mean value of altitudes at sub-grid cells, and then ($H_{sk}-H_m$) is the altitude anomaly at a sub-grid cell. Then, $\Delta CSHDSI_{mtph}$ can be referred to as the sub-grid altitude anomaly correction term for Equation 4.

The calculation of Equation 23 can be divided into offline steps (before the atmospheric model runs) and online steps (while the atmospheric model running).

Offline steps:

$$\begin{cases} f_{sk} = SF_{sk} \sum_{g=1}^{2} (MAX(cos\theta_{skg}, 0.0) \cdot A_{skg}/A_{shk}) \\ f_{mtp} = \frac{1}{N_s} \sum_{k=1}^{N_s} f_{sk} \\ \Delta f_{mtph} = \frac{1}{N_s} \sum_{k=1}^{N_s} (H_{sk} - H_m) \cdot f_{sk} \end{cases} . \quad (25)$$

Online steps:

$$\begin{cases} RDNI_{Hm} = (DNI_{mL0+500m} - DNI_{mL0})/(H_{m+500m} - H_{mL0}) \\ \Delta CSHDSI_{mtph} = RDNI_{mDH} \cdot \Delta f_{mtph} \\ CSHDSI_{mtp} \approx DNI_m \cdot f_{mtp} + \Delta CSHDSI_{mtph} \end{cases} . \quad (26)$$

In the atmospheric model, H_{mL0} is the altitude at the bottom level, H_{m+500m} is the altitude of the atmospheric model level at an altitude of about 500-meter above H_{mL0}. The 500-meter can be adjusted according to the altitude difference in the study area. $DNI_{mL0+500m}$ and DNI_{mL0} are DNI at H_{m+500m} and H_{mL0}.

3. The Plans and the Data for Verification

The validation includes the following: (1) in Taiwan Island, verifying the accuracy of 2TPA and the HPFTOA, and verifying 2FDA and 3FDA; (2) in Taiwan Island, verifying the methods of ignoring shadows and using shadowless coverage; (3) in the Qinghai-Tibet Plateau, testing the calculation speed of the HPFTOA, and verifying the deviations of several simplified schemes; (4) in the Tianshan Mountains, verifying the role of $\Delta CSHDSI_{mtph}$.

Validation 1 will evaluate the consistency of the CSHDSI with and without terrain when under a virtual vacuum atmosphere on Taiwan Island. In this scenario, there is no atmospheric absorption or scattering, so DNI_{sk} is a constant. If there is a error, it is due to the geometric algorithm of the terrain factor, which include slope β_{sk}, aspect γ_{sk} , the shading factor SF_{sk}, and A_{sk}/A_{shk}.

In this study, the DEM data with 90-meter horizontal resolution (DEM90) being used is the Shuttle Radar Topography Mission (SRTM) data with a resolution of 3 arc sec (~90 m). In this paper, the horizontal resolution of the atmospheric model is about 3 km (Model-3KM), with each grid cell containing 33×33 sub-grid cells of DEM90 data.

The DNI model (Equation 17) will be used for verification simulating.

4. Verification

4.1 The Accuracy of 2TPA, the HPFTOA, 2FDA, and 3FDA

Taiwan Island is surrounded by seas, and the Central Mountain Range extends from north to south of the island. There are 100 peaks above 3 km, and the highest peak reaches 3952m (Lai et al., 2010). This region is ideal to verify the accuracy of the CSHDSI model in complex terrain. To eliminate the interference of the surrounding islands and continent, which altitudes is set to 0.

Solar radiation is not absorbed and scattered in the virtual vacuum atmosphere. Based on the law of conservation of energy, when the solar altitude angle is greater than zero, the direct

425 solar radiation received on the land and in the shadow regions on the sea (such as the
426 shadows in the purple region in Figure 5b) would be the same as when there is no terrain.

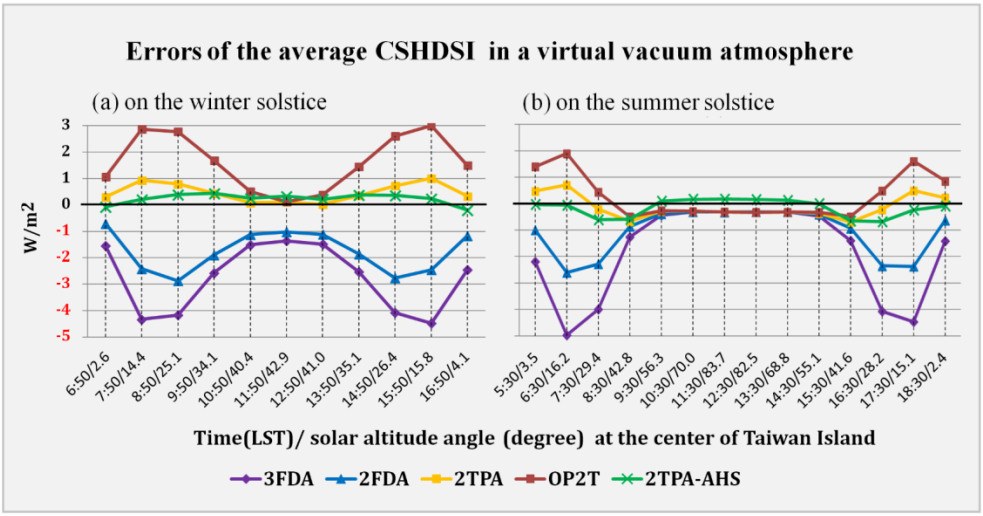

427

428 **Figure 4.** The hourly errors in the average CSHDSI of Model-3KM from 06:50 to 16:50 LST
429 on the winter solstice (a), and from 05:30 to 18:30 LST on the summer solstice (b). The average
430 CSHDSI is the mean value of all grid points within the land and shadows on the sea. The error
431 is the difference between the average CSHDSI with and without terrain. All plans are set
432 $DNI_{sk} = 1367$ W/m^2 and $D_{LC} = 1.0D_y$. OP2T: the directions of the triangle opposite to 2TPA.
433 2TPA-AHS: substituting $H'_A = 0.95\,H_A + 0.05H_{4min}$ for H_A (H_{4min} is the minimum altitude
434 of four coordinate points surrounding (i', j')) , and substituting $\beta'_{sk} = 0.998\beta_{sk}$ for β_{sk}.

435

436 Using the HPFTOA, 2TPA, 2DFA, and 3DFA, the CSHDSI with and without terrain in a
437 virtual vacuum atmosphere has been calculated on the winter solstice and the summer
438 solstice. Figure 4 shows the errors in the average CSHDSI, which is the difference between
439 the average CSHDSI with and without terrain, within the land and the shadow regions on the
440 sea. Furthermore, it is also calculated that the directions of the triangle opposite to 2TPA
441 (OP2T in Figure 4). When the altitude of the hypotenuse of the triangle is lower than the
442 average altitude H_A, the shadows calculated by H_A may be slightly less, and the CSHDSI by
443 2TPA is slightly lower when there is no shadow around noon on the summer solstice in
444 Taiwan Island, Therefore, the plans to amend the Local Altitude and slope (2TPA-AHS in
445 Figure 4) were calculated to reduce minor errors as 2TPA in Figure 4. These two conditions
446 may be related to the strong undulation of the terrain in Taiwan Island.

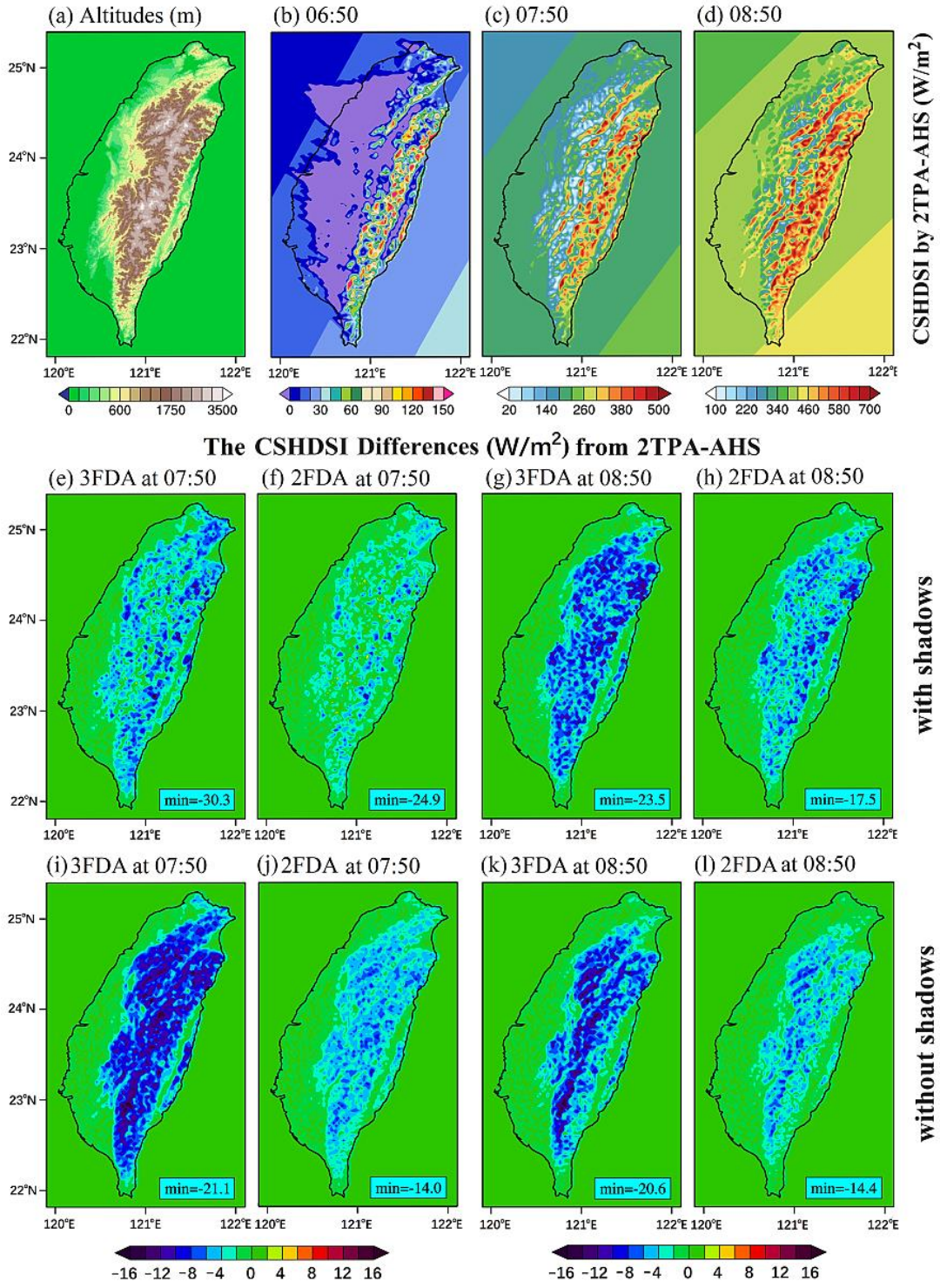

Figure 5. Altitudes (a). For 3FDA (2FDA) and 2TPA: on the winter solstice (LST), and in the Model-3KM, and taking $T_{LK0} = 2.0$, (b–d) are the CSHDSIs by 2TPA, and (e–l) are differences of CSHDSI with shadows or without shadows. In (e–l), the CSHDSI at point (i', j') (in Figure 1) of 3FDA or 2FDA is the average value of the neighboring northwest and southeast DEM data points. The "min" is the minimum value.

In Figure 4, comparing 2TPA and OP2T, it can be seen that the triangles follow the solar azimuth is very effective in reducing occlusion by the adjacent gridlines. For the hilly terrain of Taiwan Island, a slight reduction in local height and slope are also effective. For using the HPFTOA and 2TPA-AHS, the CSHDSI of the statistical region is in good agreement with that without terrain. Terrain analysis studies often use curved surfaces to simulate real terrain, as the research by Liu et al. (2004). 2TPA substitutes a plane for a curved surface. If the raised face of the curved surface in a triangle does not obscure others, the CSHDSI measured on the triangular plane is consistent with that on the curved surface. Even if this occlusion exists, it is also a displacement of radiated energy over a very short distance. The CSHDSI measured on an atmospheric model grid cell with many triangular planes should not differ significantly from with triangular curved surfaces. Therefore, the accuracy of 2TPA is highly credible. Combining with the analysis in Figure 4, it can be inferred that the accuracy of the HPFTOA is also highly credible.

In Figure 4, 2FDA and 3FDA show negative errors at solar altitude angles of 14-34°. Although the average values are low, they are mainly from the complex terrain.

Figures 5b–5l are simulated results under a real atmosphere. In Figure 5b–5d, it can be observed that the horizontal gradient of CSHDSI is very strong in Model-3KM, and the length of the longest terrain's shadow is about 100 kilometers in Figure 5b. The differences of CSHDSI between using 2FDA (3FDA) and 2TPA-AHS show there are more significant negative deviations (Figures 5e–5l). Tang et al. (2013) pointed out that the more points involved in the calculation for slope, the stronger the smoothing effect of the finite difference. Statistics show that on Taiwan Island, the proportion of DEM90 points with 3FDA, 2FDA and 2TPA slopes greater than 30° is 19.0%, 20.8% and 22.9%, respectively. Figure 6 shows that at a low solar altitude angle, a decrease in slope can cause deviations in $cos\,\theta_{sk}$. These lead to low $CSHDSI_{mt}$ in Equation 1. Because 3FDA has a stronger smoothing effect than 2FDA, it shows larger errors in Figure 4 and Figures 5e and 5g. Figure 6 can also explain why negative errors decrease at high solar altitude angles, even if the reduction of slope also results in a lower area by the actor $1/cos\,\beta_{sk}$, because the decrease in slope increases $cos\,\theta_{sk}$ at this time.

By comparing Figures 5e–h and 5i–l, it can be observed that the smoothing effect primarily occurs at the low sub-grid cells (such as the base of mountain), which is often obscured when the solar altitude angle is low. In addition, comparing Figures 5h and 5l, it can also be observed that the terrain occlusion calculated routinely in 2FDA at the grid position of DEM90 data is slightly more than 2TPA-AHS.

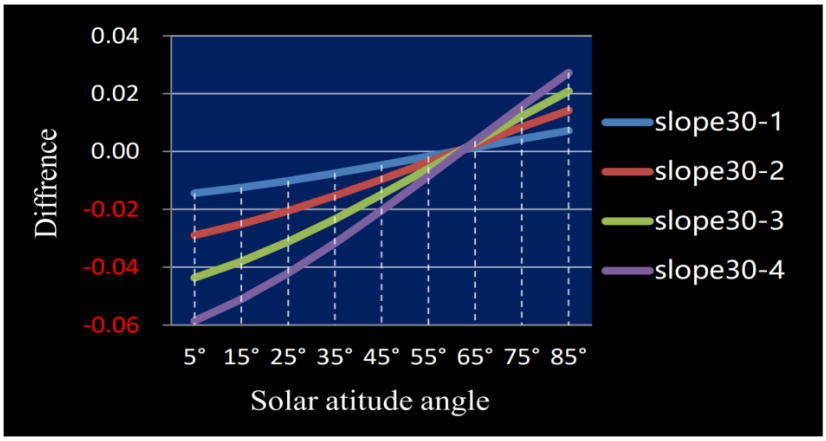

Figure 6. Changes of $cos\,\theta_{sk}$ when the slope of 15 degrees is reduced by 1, 2, 3, and 4 degrees, respectively, at different solar altitudes, assuming the slope direction is equal to the solar azimuth.

In winter, the solar altitude angle can remain low for a long time in the middle and high latitudes. Therefore, 2FDA and 3FDA method are not suitable for calculating CSHDSI in complex terrain in these regions.

4.2 The Errors of Ignoring Shadows or Using Shadowless Coverage

The methods of ignoring shadows and using shadowless coverage have been used in 2019 and beyond. These methods will be verified by being compared with the control plan in the Model-3KM. The control plan uses 2TPA-AHS, the HPFTOA, and Equations 6 and 17, and sets $T_{LK0} = 2.0$ and $D_{LC} = 1.0D_y$. The "ignoring shadows" method involves the equation $CSHDSI_{mt} = \frac{1}{N_s}\sum_{k=1}^{N_s} DNI_{sk} \cdot TCS_{sk}$. The "using SFC_m" method involves the equation $CSHDSI_{mt} = SFC_m \frac{1}{N_s}\sum_{k=1}^{N_s} DNI_{sk} \cdot TCS_{sk}$. The "correcting SFC_m" as SFC_p method

involves the equation $CSHDSI_{mt} = SFC_p \frac{1}{N_s} \sum_{k=1}^{N_s} DNI_{sk} \cdot TCS_{sk}$. The definitions of SFC_m and SFC_p are shown in Table 1.

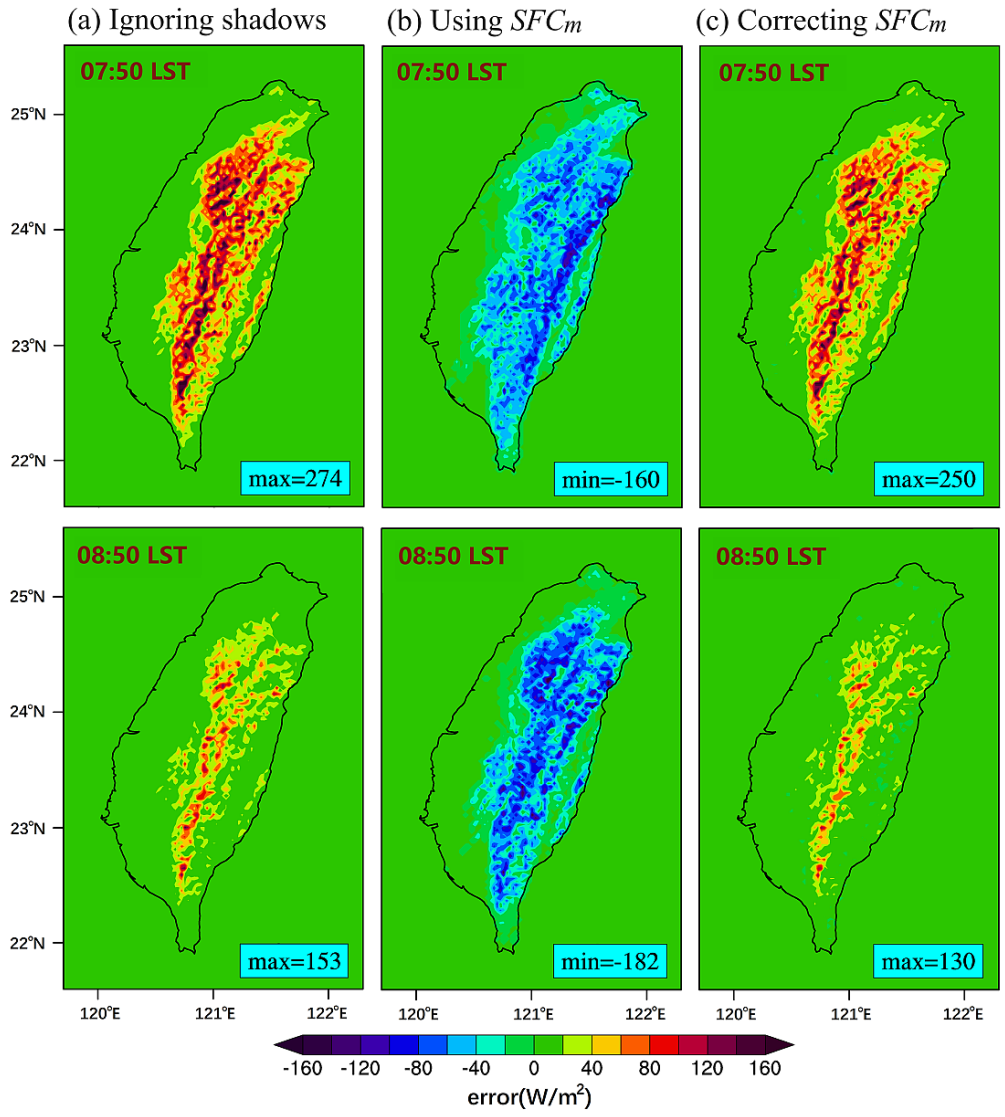

Figure 7. At 07:50 LST and 08:50 LST on the winter solstice, (a–c) are errors in $CSHDSI_{mt}$ of ignoring shadows, and using shadowless coverage SFC_m, and correcting SFC_m as SFC_p. All of them use the HPFTOA, 2TPA and take $T_{LK0} = 2.0$. The "max" and "min" are the maximum and the minimum value of the errors, respectively. The definitions of SFC_m and SFC_p are shown in Table 1.

Figure 7 shows the errors distribution at two moments. The errors are too big relative to the value in Figures 5c–5d. Since some shadows with low $cos\,\theta_{sk}$ (self-occlusion, etc.) are counted into SFC_m, using SFC_m must result in negative biases in CSHDSI (Huang et al.,

2022). The errors of using SFC_m are not uniform (Figures 8b and 8f), so correcting SFC_m as SFC_p by a linear factor (Huang et al., 2022) does not solve the problem of errors. At that time, solar altitude angles of the central point of Taiwan Island are 14.4° and 25.1°, indicating that these three methods are especially unsuitable for the middle and high latitudes.

4.3 The Calculation Speed of the HPFTOA

According to the plans outlined in Table 2, the calculation speed of the HPFTOA was tested in the eastern part of the Tibet Plateau (84.68°–105.32°E, 24.68°–40.32°N) (Figure 8a). Mount Everest (86°55’31’’ E, 27°59’17’’ N) is located within the blue rectangle. The largest difference in every simplification plan in Model-3KM is analyzed. The plan SUTSM is the same as that of Huang et al. (2022).

Table 2. The test plans and results in the eastern part of the Qinghai-Tibet Plateau*

Plan	Time (minutes) spent on calculation					Maximum difference (W/m2)
	08:00	09:00	10:00	13:00	Daytime	
$D_{LC} = 1.0D_y$	1.85	6.73	3.89	2.02	40.12	/
$D_{LC} = 1.5D_y$	1.40	5.32	3.80	2.01	36.90	3.4
$D_{LC} = 2.5D_y$	1.03	4.20	3.69	2.01	34.60	4.4
$D_{LC} = 5.0D_y$	0.81	3.45	3.62	2.02	32.28	-10.82
SUTSM	0.30	1.58	2.72	1.95	24.24	-357.4

* The time spent on calculating slope, slope direction, area, solar position, and occlusion at 08:00, 09:00, 10:00, and 13:00 LST, as well as during the daytime (08:00–19:00 LST) on the winter solstice; the maximum difference of CSHDSI in Model-3KM between the plans and the plan $D_{LC} = 1.0D_y$. The SUTSM acronym stands for the simultaneous use of three simplified methods. Three simplified methods are taking the lowest solar altitude angle $\alpha_0 = 0$, ignoring the earth's curvature, and using the fixed search occlusion radius of 27 km. All plans take $T_{LK0} = 2.0$, and use 2TPA and DEM90 data.

The area of Figure 8a is divided into 10x8 small rectangles to speed up the calculation. Based on the location of this region, judging pole and converting positive-negative longitude in Equation 15 are ignored. The testing computing server is equipped with two Intel (R) Xeon (R) Gold 6132 CPUs (14 cores, @2.60GHz), 128GB of RAM, a Linux operating system, and

549 the Intel (R) Fortran compiler version 2021.5.0. This server is very common. The OMP
550 parallel computation uses 26 threads. The testing results are presented in Table 2.
551

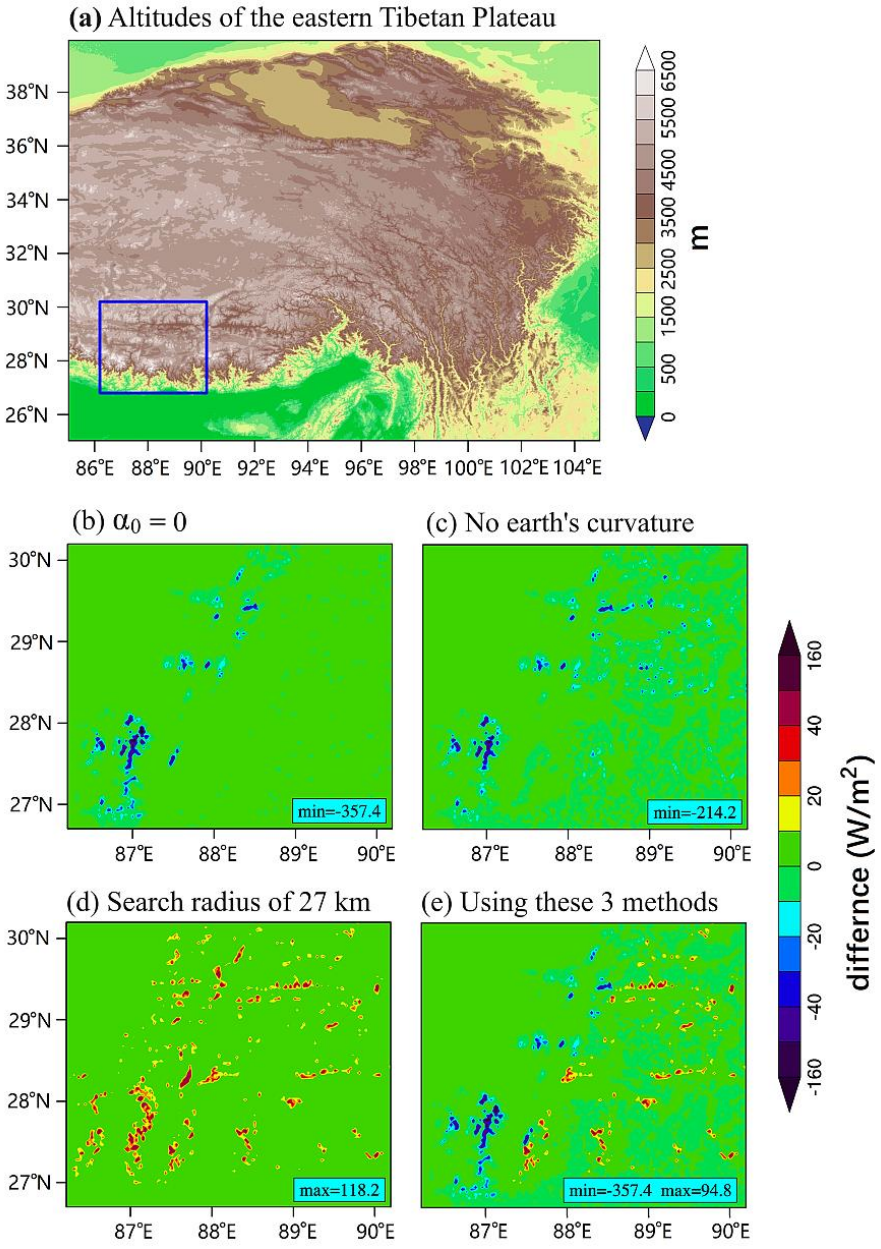

552
553 **Figure 8.** Altitudes of the eastern Tibetan Plateau (a); differences of CSHDSI in the
554 Model-3KM between the three simplified methods and the plan $D_{LC} = 1.0D_y$ (b–e).
555 The "max" and "min" is the maximum and the minimum value of the differences,
556 respectively.
557

During the daytime, the time required to calculate one of the plans $D_{LC} = 1.0D_y, 1.5D_y$, and $2.5D_y$ increases by 0.41 to 0.66 times compared to using three simplified methods. In an area of less undulating terrain, because of the decrease in search occlusion radius, it can be expected that the increase in the HPFTOA calculation time will be reduced, or even faster than a fixed search occlusion radius of 27 km. This calculation cost is perfectly acceptable for institutions conducting numerical atmospheric simulations. The loss of accuracy in the plan $D_{LC} = 2.5D_y$ is minimal. This plan is equivalent to using 225-meter horizontal resolution DEM data to calculate occlusion at a far distance. When calculating far terrain occlusion, the sparse DEM data can be used after testing.

Figure 8b-8e (locating in the blue rectangle in Figure 8a) shows the differences between the three simplified methods and the plan $D_{LC} = 1.0D_y$. It can be seen that the simplified methods has large deviations in some areas. Although these is very short (a few minutes), it can last for a longer time at high latitudes, and the atmospheric refraction effect also prolongs which.

The verification in this section shows that the calculation cost of using the HPFTOA is feasible.

4.4 The Role of $\Delta CSHDSI_{mtph}$

The role of $\Delta CSHDSI_{mtph}$ is verified in the middle part (Figure 9d) of the Tianshan Mountains (Figure 9c). The Tianshan Mountains are nearby six deserts. The turbid weather often occurs there. The errors in $CSHDSI_{mtp}$ by using or not using $\Delta CSHDSI_{mtph}$ are compared in general and turbid weather ($T_{LK0} = 3.0$ and 6.0). All of these use the HPFTOA, 2TPA and $D_{LC} = 1.0D_y$. The times are from 10:40 LST to 18:40 LST during the 1-hour interval of the winter solstice.

The results show that when using $\Delta CSHDSI_{mtph}$, the maximum absolute error during the daytime is less than 2.3 W/m2. When not using $\Delta CSHDSI_{mtph}$, the maximum absolute error of can reach 23.3 W/m2 in the turbid weather ($T_{LK0} = 6.0$). In Figures 10a and 10b, it can be

observed that not using $\Delta CSHDSI_{mtph}$ mainly lead to negative errors, which increases in turbid weather than general weather ($T_{LK0} = 3.0$).

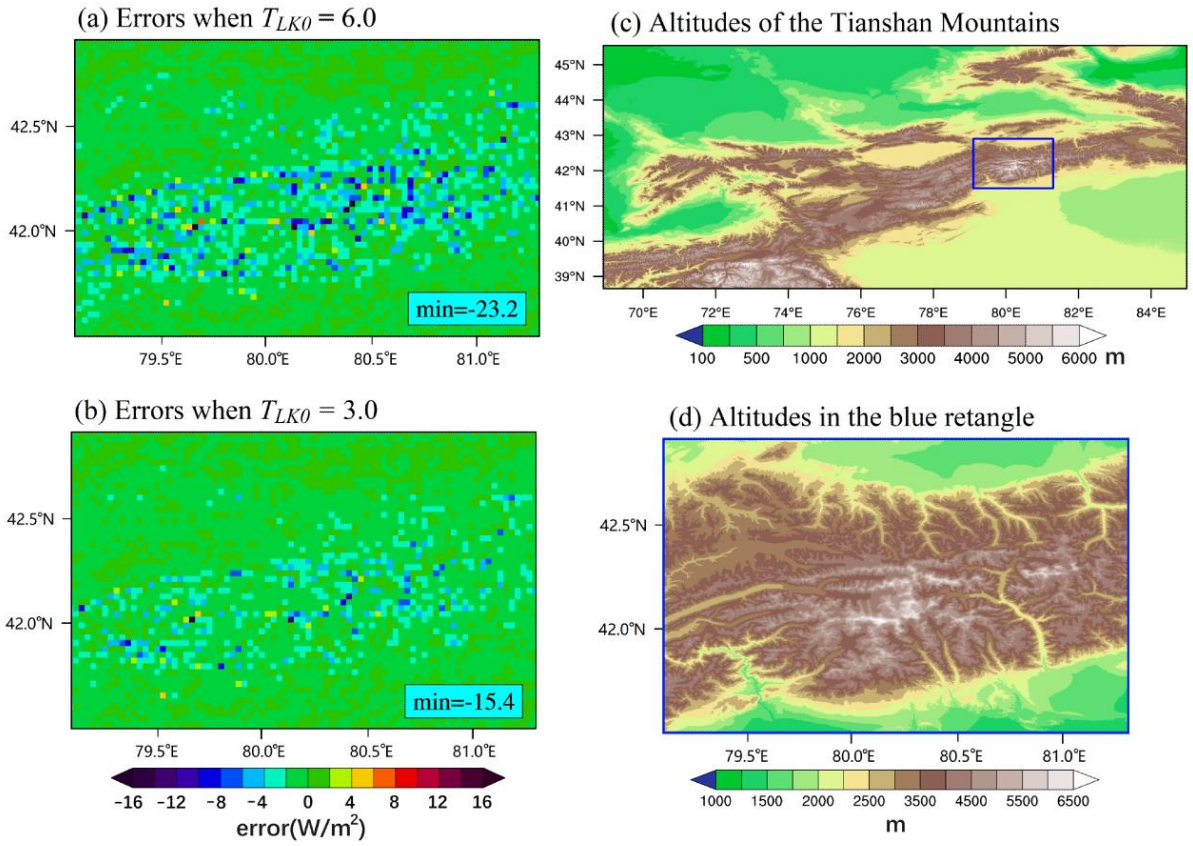

Figure 9: Errors in $CSHDSI_{mtp}$ at 11:40 LST on the winter solstice when not using $\Delta CSHDSI_{mtph}$ (a–b), and the "min" is the minimum value of errors. Altitudes of the Tianshan Mountains (c) and in the blue rectangle (d).

Since $\frac{1}{N_s}\sum_{k=1}^{N_s}(H_{sk}-H_m) = 0$, when CSHDSI is distributed randomly with altitude, $\Delta CSHDSI_{mtph} \approx 0$, and this is equivalent to Equation 4. However, because the shadow often appears at a low place, not using $\Delta CSHDSI_{mtph}$ mainly presents a negative error.

This also reminds us that H_m and H_{sk} must meet the condition $\frac{1}{N_s}\sum_{k=1}^{N_s}(H_{sk}-H_m) = 0$ for SPS-CSDSR. Otherwise, no matter using Equation 4 or Equation 23 for parameterization, unexpected deviations are brought about. Therefore, it is necessary to unify the altitude data sources of atmospheric model and SPS-CSDSR.

606

607

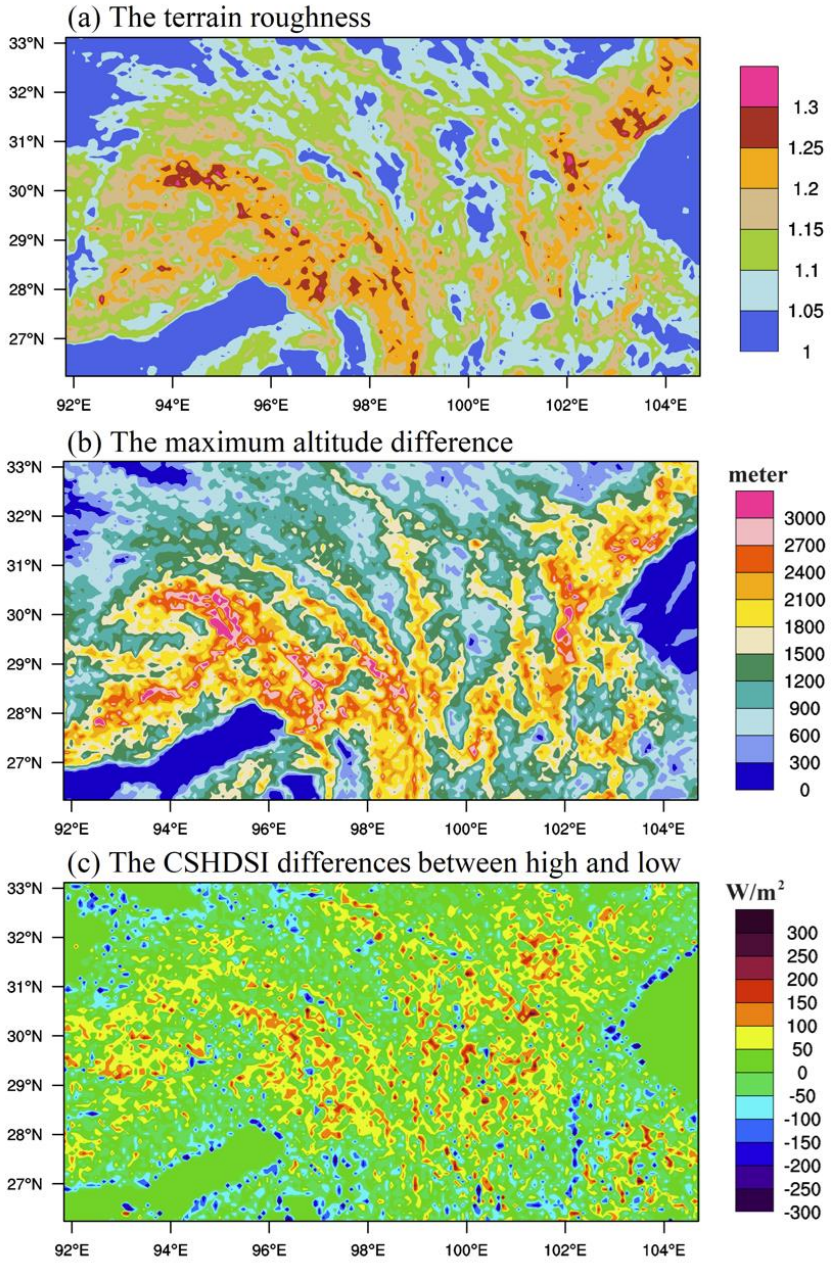

608

609 **Figure 10.** In an atmospheric model with a horizontal resolution of 9 km (97×97 DEM90 grid cells),
610 and at 10:00 LST on the summer solstice, the following parameters were calculated: the terrain
611 roughness (a) calculated by using 2TPA, the maximum altitude difference (b) within a grid cell, and
612 the CSHDSI differences (c) between above (high) and below (low) the average altitude. All used
613 2TPA-HPFTOA, with $T_{LK0} = 2.0$, and measured high and low CSHDSI on the full area of the grid
614 cell. When the maximum altitude difference is less than 600 meters, the CSHDSI difference in an
615 atmospheric model is set to zero.

5 Conclusion and Discussion

The verification shows that the existing SPS-CSDSRs use a small search occlusion radius and the common finite difference slope algorithms, ignore shadows or use shadowless coverage, and assume consistent DNI of sub-grid cells within an atmospheric model grid cell, all of which can lead to significant errors in the Model-3KM. This renders existing SPS-CSDSRs unsuitable for complex terrain in middle and high latitudes and in turbid weather. Of course, the size of these errors in the horizontal plane also depends on the horizontal resolution of the atmospheric model. In the undulating mountains, the distributions of terrain effects are scattered, as are their errors. When the atmospheric model's horizontal resolution is reduced (such as Huang's study in 2022), they are smoothed in the horizon plane, and the errors become smaller. Instead, it can be amplified. At present, many weather forecasting models with a horizontal resolution of 3km are in operation at national meteorological agencies. For example the CMA-MESO and the High-Resolution Rapid Refresh (HRRR) of NOAA. Therefore, verifications in this paper with a horizontal resolution of 3 km are appropriate.

Even if these errors are small in the horizontal grid cells of the atmospheric model, they should not be ignored when introducing sub-grid terrain effects at different heights of the atmospheric model. Existing land surface physical models are designed for flat ground, using real physical parameters such as aerodynamic roughness and emissivity of the surface, heat capacity of the soil, etc. The current practice of directly coupling the terrain effects on solar radiation into the horizontal plane of the land surface model needs to be improved, as the area size and altitude of the received solar radiation deviate from the real situation. For example, in an atmospheric model with a horizontal resolution of 9 km (97×97 DEM90 grid cells), and in the south-east part of the Qinghai-Tibet Plateau, the terrain roughness (ratio of surface area to horizontal area) of many grid points are above 1.2 (Figure 10a), and the land relief in a grid cell can reach 3000 meters (Figure 10b). In complex terrain, most high sub-grid cells receive more direct solar radiation than the low ones (Figure 10c). Therefore, it is necessary to make reasonable improvements in the land-air physical process and vertical

distribution rather than simply coupling to the horizontal plane. Improvements in the vertical distribution require raising the horizontal resolution of the atmospheric model, or introducing sub-grid terrain effects at different heights of the atmospheric model. This is important for improving the accuracy of simulating the high influence factors on radiation, such as snow cover, frozen soil, and terrain clouds (fogs). In this case, the three improvements of this study will play a key role because those errors at the atmospheric model grid mainly occur in the lower sub-grid cells.

This study also notes that some coupled simulation studies incorporated solar irradiance on the slope plane into the horizontal plane of the atmospheric model, or ignored the A_{sk}/A_{shk} factors of the sub-grid when parameterizing. As a result, the total solar radiation in regions with high terrain roughness (such as those shown in Figure 10a) will be significantly underestimated. Therefore, in this paper, the acronym "CSHDSI" has been used in the equations to prevent confusion and to help clarify this issue.

The three improvements in this study effectively avoid the errors of the existing SPS-CSDSRs. 2TPA avoids the errors caused by the finite difference algorithms, and the HPFTOA solves the problems of calculation accuracy and speed. These two improvements made the direct solar radiation model with the most precise geometric algorithm to date and suitable for terrain at any latitude. The sub-grid altitude anomaly correction term reduces errors in parameterization, letting SPS-CSDSR adapt to the turbid weather in complex terrain. These have improved all four factors that can lead to errors in Equations 2–3 and constitute a high-precision SPS-CSDSR in complex terrain in the atmospheric model. Evaluating the consistency of CSHDSI with and without terrain in a virtual vacuum atmosphere is a successful endeavor. By this way, the accuracy of the proposed schemes is confirmed, and the systematic deviations by the second- and third-order finite difference slope algorithms for direct solar radiation are identified.

Evaluating the consistency of direct solar radiation with and without terrain in a virtual vacuum atmosphere is a successful endeavor is a successful endeavor. Through this approach, the deviation of the geometric algorithm for direct solar radiation can be identified and used

to adjust the adaptability of the geometric model to terrain features, such as local altitude. This is particularly important for accurate calculations of the CSHDSI for a specific area, as shown in 2TPA-AHS in Figure 4. When the horizontal resolution of the DEM data is not 90 meters that for this study, it is recommended to also use this method for testing.

The methods for reducing calculations in Table 1 began in 1990. Although the performance of the computer has been greatly improved, these practices continued to before this study. This paper has verified that seven of these methods can lead to significant errors, and the problems with other methods are also obvious. The methods of ignoring shadows or using a small search occlusion radius and shadowless coverage are still in use after 2019, and the large errors led by them have not been paid attention to. This paper has clarified that the HPFTOA's skill and computer advances can make all methods in Table 1 no longer be used.

The evaluation of calculation costs in this study is based on 90-meter horizontal resolution DEM data. For the higher-horizontal resolution DEM data, the preliminary research conclusion is that the DEM data can be sparse with only a small loss of accuracy when calculating the far terrain occlusion. The specific scheme can be determined by comparing the accurate scheme.

In terms of subject classification, 2TPA and the HPFTOA should belong to the field of solar radiation modeling. Although there have been more than 20 solar radiation models (introduced by Yang (2016)) for inclined surfaces, HPFTOA and the problem of the finite difference slope algorithms have been neglected, but these are important for atmospheric physical processes. Since some parameters of the scattering or reflection model are related to slope and direct solar irradiance, we are not yet sure of the accuracy of these highly ranked models (ranked by Yang (2016)) when using 2TPA instead of finite difference or direct solar irradiance by 2TPA-HPFTOA. Therefore, these effects need to be evaluated when the algorithms and schemes presented in this paper are used to calculate the total solar radiation.

Acknowledgments

This study is supported by funds from the China Meteorological Administration Innovation Development Project (CXFZ2023P023) and the project (ZR2022MD040) of the Shandong Provincial Natural Science Foundation. The authors are grateful to NASA, Intel®, and NCAR for allowing us to freely use the data and software.

Data Availability Statement

The DEM data used in this study is the Shuttle Radar Topography Mission (SRTM) 90m Digital Elevation Database v4.1 (Jarvis et al., 2008, https: //developers. google.com/earth-engine/datasets/catalog/CGIAR_SRTM90_V4). Figures 4, 11, and 13 are based on this data.

The program that calculates based on DEM90 data is written in Fortran 90 and compiled using the ifort compiler (version 2021.5.0) from Intel® Fortran, which is available at no cost. This compiler is part of the Intel® oneAPI Toolkits products for Linux. The latest no-cost version can be downloaded by connecting to https://www.intel.com/content/www/us/en/developer/articles/news/free-intel-software-developer-tools.html. The NCL version 6.4.0 https://www.ncl.ucar.edu/prev_releases.shtml - 6.4.0) was used to convert the result in DEM90 data grid to a Model-3KM for analytical testing. Figures 4 and 6 and 7 and 8 and 10 and 11 and 13 and 14 and 15 were made with NCL version 6.4.0.

The DEM data and source codes of this manuscript can be accessed online (https://doi.org/10.5281/zenodo.10446114).

References

Cai, S., Huang, A., Zhu, K., Guo, W., Wu, Y., & Gu, C. (2023). The forecast skill of the summer precipitation over Tibetan Plateau improved by the adoption of a 3D sub-grid terrain solar radiative effect scheme in a convection-permitting model. *Journal of Geophysical Research: Atmospheres*, 128(11), e2022JD038105. https://doi.org/10.1029/2022JD038105

Dozier, J. F., & Frew, J. (1990). Rapid calculation of terrain parameters for radiation modeling from digital elevation data. *IEEE Transactions on Geoscience and Remote Sensing*, 28(5), 963‐969. https://doi.org/10.1109/36.58986

Dubayah, R., Dozier, J., & Davis, F. W. (1990). Topographic distribution of clear-sky radiation over the Konza Prairie, Kansas. *Water Resources Research*, 26(4), 679‐690. https://doi.org/10.1029/WR026i004p00679

Dubayah, R., & Rich, P. M. (1995). Topographic solar radiation models for GIS. International *Journal of Geographical Information Systems*, 9(4), 405-419. https://doi.org/10.1080/02693799508902046

Ed, W. (2013). Lat/lon given radial and distance. Aviation Formulary V1.47 (http://www.edwilliams.org/avform147.htm - LL).

Essery, R., & Marks, D. (2007). Scaling and parametrization of clear-sky solar radiation over complex topography. *Journal of Geophysical Research: Atmospheres*, 112, D10122. https://doi.org/10.1029/2006JD007650

Fu, P. (2000). A geometric solar radiation model with applications in landscape ecology. University of Kansas, Lawrence, Kansas, USA.

Gu, C., Huang, A., Wu, Y., Yang, B., Mu, X., Zhang, X., & Cai, S. (2020). Effects of sub-grid terrain radiative forcing on the ability of RegCM4.1 in the simulation of summer precipitation over China. *Journal of Geophysical Research: Atmospheres*, 125(12), e2019JD032215. https://doi.org/10.1029/2019JD032215

Gu, C., Huang, A., Zhang, Y., Yang, B., Cai, S., Xu, X. Luo, J., & Wu, Y. (2022). The wet bias of RegCM4 over Tibet Plateau in summer reduced by adopting the 3D sub-grid terrain solar radiative effect parameterization scheme. *Journal of Geophysical Research: Atmospheres*, 127(21), e2022JD037434. https://doi.org/10.1029/2022JD037434

Hao, D., Bisht, G., Gu, Y., Lee, W. L., Liou, K. N., & Leung, L. R. (2021). A parameterization of sub-grid topographical effects on solar radiation in the E3SM land model (version 1.0): implementation and evaluation over the Tibetan plateau. *Geoscientific Model Development*, 14(10), 6273‐6289. https://doi.org/10.5194/gmd-14-6273-2021

He, S., Smirnova, T. G., & Benjamin, S. G. (2019). A scale-aware parameterization for estimating sub-grid variability of downward solar radiation using high-resolution digital

771 elevation model data. *Journal of Geophysical Research: Atmospheres*, 124(24), 13680-
772 13692. https://doi.org/10.1029/2019JD031563
773 Helbig, N., & Löwe, H. (2012). Shortwave radiation parameterization scheme for sub-grid
774 topography. *Journal of Geophysical Research: Atmospheres*, 117, D03112.
775 https://doi.org/10.1029/2011JD016465
776 Hofierka, J., & Kaňuk, J. (2009). Assessment of photovoltaic potential in urban areas using
777 open-source solar radiation tools. *Renewable Energy*, 34(10), 2206 - 2214.
778 https://doi.org/10.1016/j.renene.2009.02.021
779 Hofierka, J., & Suri, M. (2002). The solar radiation model for Open source GIS:
780 implementation and applications, paper presented at Proceedings of the Open Source GIS-
781 Grass Users Conference, Università degli studi di Trento, Trento, Italy.
782 Huang, A., Gu, C., Zhang, Y., Li, W., Zhang, J., Wu, Y. Zhang, X., & Cai, S. (2022).
783 Development of a clear-sky 3D sub-grid terrain solar radiative effect parameterization
784 scheme based on the mountain radiation theory. *Journal of Geophysical Research:*
785 *Atmospheres*, 127(13), e2022JD036449. https://doi.org/10.1029/2022JD036449
786 Jarvis, A., Reuter, H. I., Nelson, A., & Guevara, E. (2008). The Shuttle radar topography
787 mission (SRTM) 90m digital elevation Database v4.1 [Dataset]. International Centre for
788 Tropical Agriculture (CIAT). Retrieved from https://developers.google.com/earth-
789 engine/datasets/catalog/ CGIAR_SRTM90_V4.
790 Kasten, F. (1996). The Linke turbidity factor based on improved values of the integral
791 Rayleigh optical thickness. *Solar Energy*, 56(3), 239-244. https://doi.org/10.1016/0038-
792 092X(95)00114-7
793 Kasten, F., & Young, A. T. (1989). Revised optical air mass tables and approximation
794 formula. *Applied Optics*, 28(22), 4735-4738. https://doi.org/10.1364/AO.28.004735
795 Kondratyev, K. Y. (1977). Radiation regime of inclined surfaces. *Technical Report Rep*. N-
796 79-11613, 82 pp, World Meteorological Organization, United States.
797 Kumar, L. Skidmore, A. K., & Knowles, E. (1997). Modelling topographic variation in solar
798 radiation in a GIS environment. *International Journal of Geographical Information*
799 *Science*, 11(5), 475-497. https://doi.org/10.1080/136588197242266

Lai, Y.-J., Chou, M.-D., & Lin, P.-H. (2010). Parameterization of topographic effect on surface solar radiation. *Journal of Geophysical Research: Atmospheres*, 115, D01104. https://doi.org/10.1029/2009JD012305

Li, Z. Q., & Weng, D. M. (1987). A computer model to determine topographic parameters (Chinese with English abstract). *Acta Geographica Sinica*, 42(3), 269-278. https://doi.org/10.11821/xb198703009

Liu, X. Gong, J., Zhou, Q., & Tang, G. (2004). A study of accuracy and algorithms for calculating slope and aspect based on grid digital elevation model (DEM). *Acta Geodaetica et Cartographica Sinica*, 33(3), 258-263. doi:10.3321/j.issn:1001-1595.2004.03.014

Müller, M. D., & Scherer, D. (2005). A grid- and sub-grid-scale radiation parameterization of topographic effects for mesoscale weather forecast models. *Monthly Weather Review*, 133(6), 1431‑1442. https://doi.org/10.1175/MWR2927.1

Neteler, M., & Mitasova, H. (2008). Open source Gis: A GRASS GIS approach. Third edition ed., *Springer Science Business Media*, New York. https://doi.org/10.1007/978-0-387-68574-8

Nguyen, H. T., & Pearce, J. M. (2010). Estimating Potential Photovoltaic Yield with *r.sun* and the Open-Source Geographical Resources Analysis Support System. *Solar Energy*, 84(5), 831-843. https://doi.org/10.1016/j.solener.2010.02.009

Pintor, B. H., Sola, E. F., Teves, J., Inocencio, L. C., Ang, M. R. C., & Concepcion, R. (2015). Solar energy resource assessment using R. SUN in GRASS GIS and site suitability analysis using AHP for groundmounted solar photovoltaic (Pv) farm in the Central Luzon Region (Region 3), Philippines. Free and open source software for geospatial (Foss4g) Conference Proceedings, Seoul, South Korea. https://doi.org/10.7275/R5N58JKF

Remund, J., Wald, L., Lefèvre, M., Ranchin, T., & Page, J. H. (2003). Worldwide Linke turbidity information. ISES Solar World Congress 2003, Göteborg, Sweden, Jun 2003.

Rigollier, C., Bauer, O., & Wald, L. (2000). On the clear-sky model of the ESRA - European Solar Radiation Atlas - with respect to the Heliosat method. *Solar Energy*, 68(1), 33-48. https://doi.org/10.1016/S0038-092X(99)00055-9

Ruiz-Arias, J. A., Tovar-Pescador, J., Pozo-Vázquez, D., & Alsamamra, H. (2009). A comparative analysis of DEM-based models to estimate the solar radiation in mountainous terrain. *International Journal of Geographical Information Science*, 23(8), 1049‑1076. https://doi.org/10.1080/13658810802022806

Sharpnack, D. A., & Akin, G. (1969). An algorithm for computing slope and aspect from elevations. *Photogrammetric Engineering*, 35(3), 247‑248. https://www.asprs.org/wp-content/uploads/pers/1969journal/mar/1969_mar_247-248.pdf

Swift, L. W. (1976). Algorithm for solar radiation on mountain slopes. *Water Resources Research*, 12(1), 108-112. https://doi.org/10.1029/WR012i001p00108

Tang, J., Pilesjö, P., & Persson, A. (2013). Estimating slope from raster data ‑ a test of eight algorithms at different resolutions in flat and steep terrain. *Geodesy and Cartography*, 39(2), 41‑52. https://doi.org/10.3846/20296991.2013.806702

Yang, D. Z. (2016). Solar radiation on inclined surfaces: Corrections and benchmarks. Solar Energy. 136. 288-302. https://doi.org/10.1016/j.solener.2016.06.062

Yue, S., Yang, K., Lu, H., Zhou, X., Chen, D., & Guo, W. (2021). Representation of stony surface-atmosphere interactions in WRF reduces cold and wet biases for the southern Tibetan Plateau. *Journal of Geophysical Research: Atmospheres*, 126(21), e2021JD035291. https://doi.org/10.1029/2021JD035291

Zhang, X., Huang, A., Dai, Y., Li, W., Gu, C., Yuan, H., Wei, N., Zhang, Y., Qiu, B., & Cai, S. (2022). Influences of 3D sub-grid terrain radiative effect on the performance of CoLM over Heihe River Basin, Tibetan Plateau. *Journal of Advances in Modeling Earth Systems*, 14(1), e2021MS002654. https://doi.org/10.1029/2021MS002654

Zhang, Y., Huang, A., & Zhu, X. (2006). Parameterization of the thermal impacts of sub-grid orography on numerical modeling of the surface energy budget over East Asia. *Theoretical and Applied Climatology*, 86(1-4), 201‑214. https://doi.org/10.1007/s00704-005-0209-1

Zhou, Z. W., XIONG, J. J., & HUANG, Y. Y. (2013), Method for Determination of Radar Terrain Masking Blind Zone Based on DEM (Chinese with English abstract). *Journal of Air & Space Early Warning Research,* 27(05), 327-330

Figure 1.

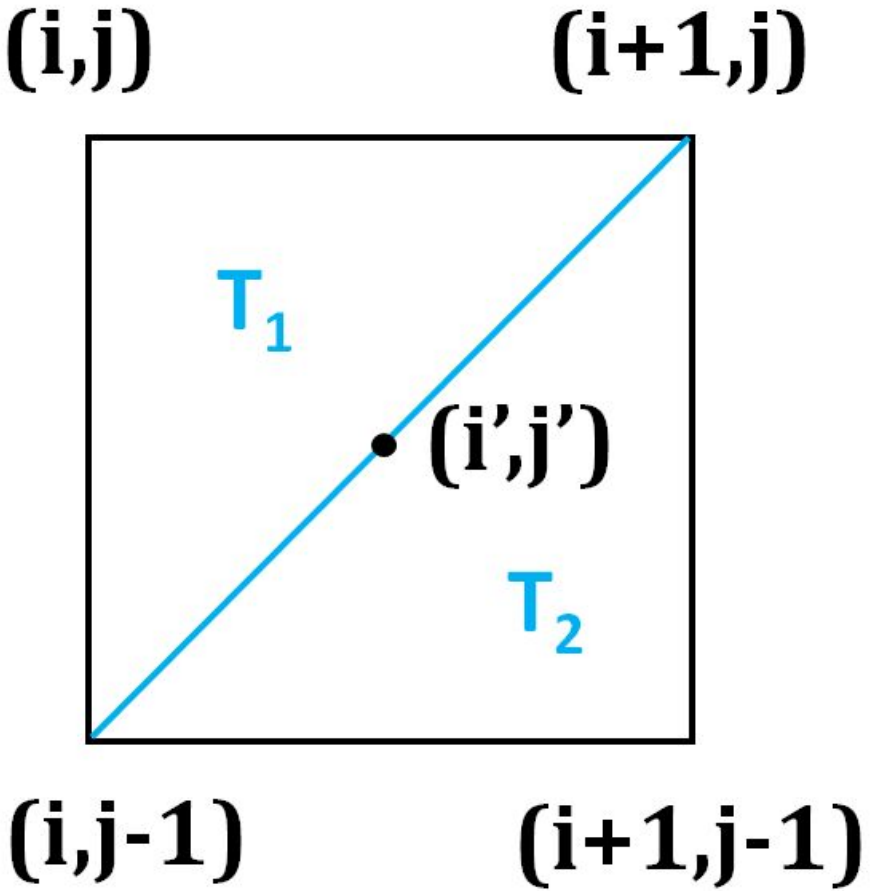

$tan\varphi_{sk} \geq 0$

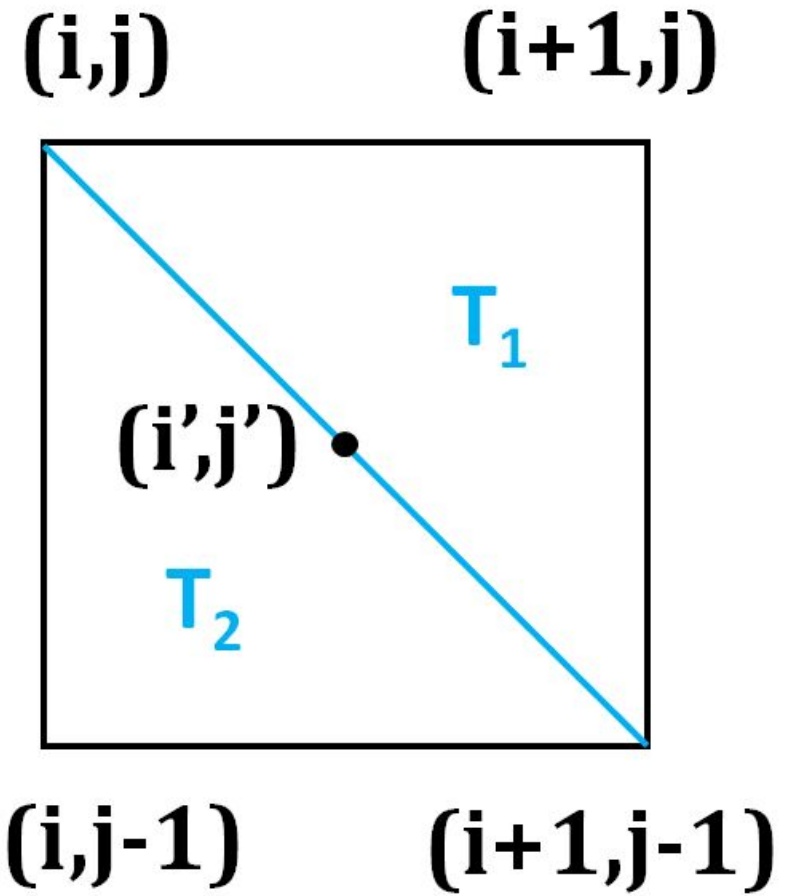

$tan\varphi_{sk} < 0$

Figure 2.

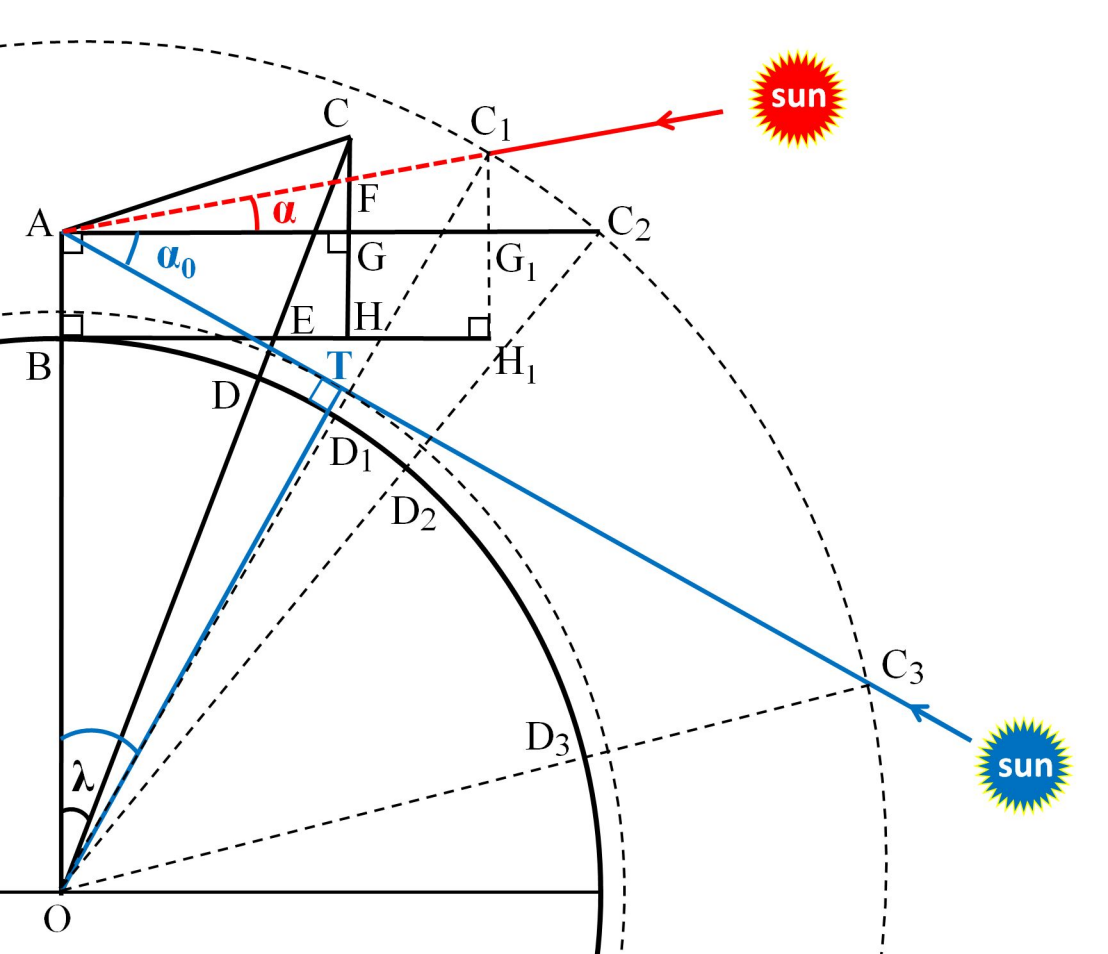
sun
C
C1
A
α
F
C2
α0
G
G1
E
H
B
H1
T
D
D1
D2
C3
D3
sun
λ
O

Figure 3.

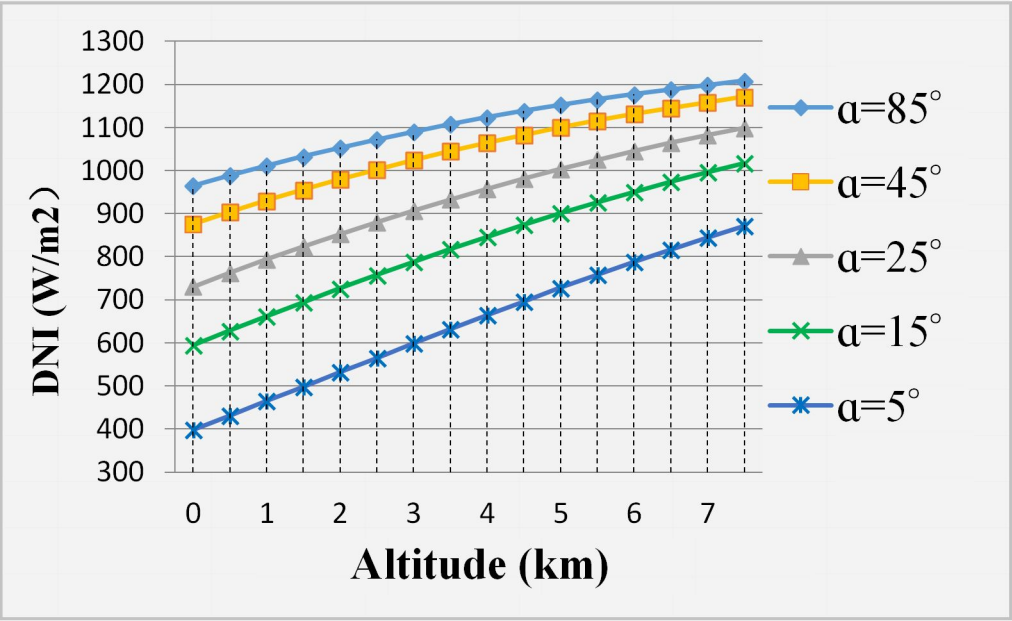
1300
1200
1100
1000
900
800
700
600
500
400
300
DNI (W/m2)
0
1
2
3
4
5
6
7
Altitude (km)
α=85°
α=45°
α=25°
α=15°
α=5°

Figure 4.

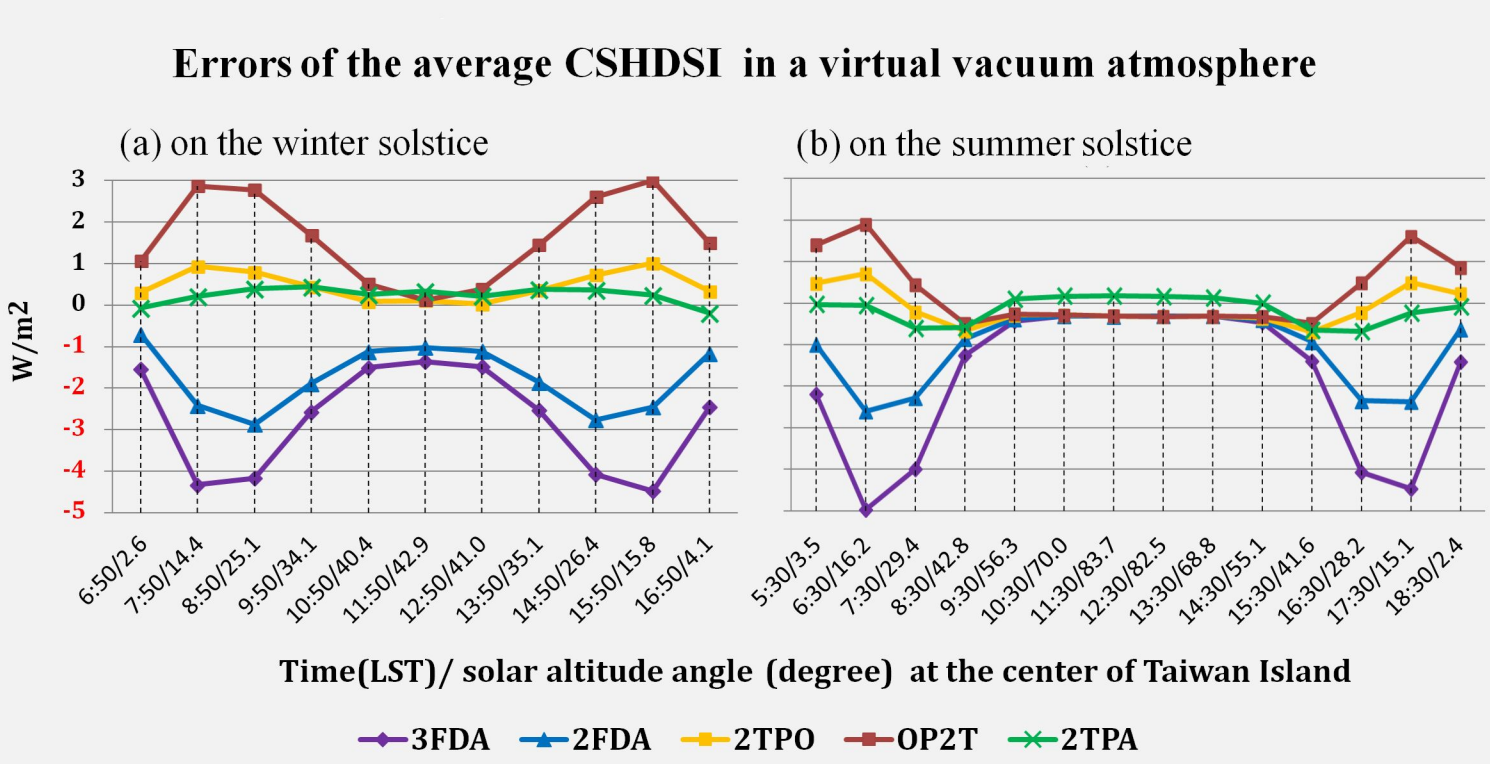
Errors of the average CSHDSI in a virtual vacuum atmosphere
(a) on the winter solstice
(b) on the summer solstice
W/m2
3
2
1
0
-1
-2
-3
-4
-5
6:50/2.6
7:50/14.4
8:50/25.1
9:50/34.1
10:50/40.4
11:50/42.9
12:50/41.0
13:50/35.1
14:50/26.4
15:50/15.8
16:50/4.1
5:30/3.5
6:30/16.2
7:30/29.4
8:30/42.8
9:30/56.3
10:30/70.0
11:30/83.7
12:30/82.5
13:30/68.8
14:30/55.1
15:30/41.6
16:30/28.2
17:30/15.1
18:30/2.4
Time(LST)/ solar altitude angle (degree) at the center of Taiwan Island
3FDA
2FDA
2TPO
OP2T
2TPA

Figure 5.

(a) Altitudes (m)

(b) 06:50

(c) 07:50

(d) 08:50

25°N
24°N
23°N
22°N

120°E 121°E 122°E

0 600 1750 3500

0 30 60 90 120 150

20 140 260 380 500

100 220 340 460 580 700

CSHDSI by 2TPA-AHS (W/m^2)

The CSHDSI Differences (W/m^2) from 2TPA-AHS

(e) 3FDA at 07:50

(f) 2FDA at 07:50

(g) 3FDA at 08:50

(h) 2FDA at 08:50

min=-30.3

min=-24.9

min=-23.5

min=-17.5

with shadows

(i) 3FDA at 07:50

(j) 2FDA at 07:50

(k) 3FDA at 08:50

(l) 2FDA at 08:50

min=-21.1

min=-14.0

min=-20.6

min=-14.4

without shadows

-16 -12 -8 -4 0 4 8 12 16

Figure 6.

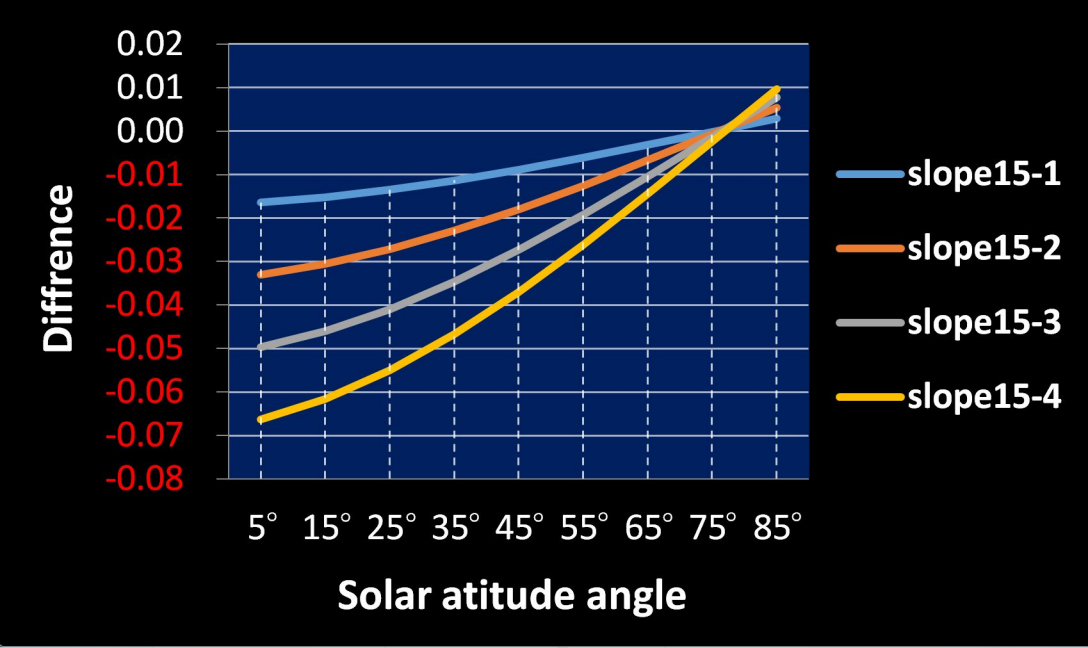
0.02
0.01
0.00
-0.01
-0.02
-0.03
-0.04
-0.05
-0.06
-0.07
-0.08
Diffrence
5°
15°
25°
35°
45°
55°
65°
75°
85°
Solar atitude angle
slope15-1
slope15-2
slope15-3
slope15-4

Figure 7.

(a) Ignoring shadows

(b) Using *SFCm*

(c) Correcting *SFCm*

07:50 LST

07:50 LST

07:50 LST

max=274

min=-160

max=250

08:50 LST

08:50 LST

08:50 LST

max=153

min=-182

max=130

25°N

24°N

23°N

22°N

120°E

121°E

122°E

-160 -120 -80 -40 0 40 80 120 160

error(W/m^2)

Figure 8.

(a) Altitudes of the eastern Tibetan Plateau

38°N
36°N
34°N
32°N
30°N
28°N
26°N
86°E 88°E 90°E 92°E 94°E 96°E 98°E 100°E 102°E 104°E
m
6500 5500 4500 3500 2500 1500 500 0

(b) $\alpha_0 = 0$

30°N
29°N
28°N
27°N
87°E 88°E 89°E 90°E
min=-357.4

(c) No earth's curvature

87°E 88°E 89°E 90°E
min=-214.2

(d) Search radius of 27 km

30°N
29°N
28°N
27°N
87°E 88°E 89°E 90°E
max=118.2

(e) Using these 3 methods

87°E 88°E 89°E 90°E
min=-357.4 max=94.8

difference (W/m^2)
160 40 20 0 -20 -40 -160

Figure 9.

(a) Errors when T_{LK0} = 6.0

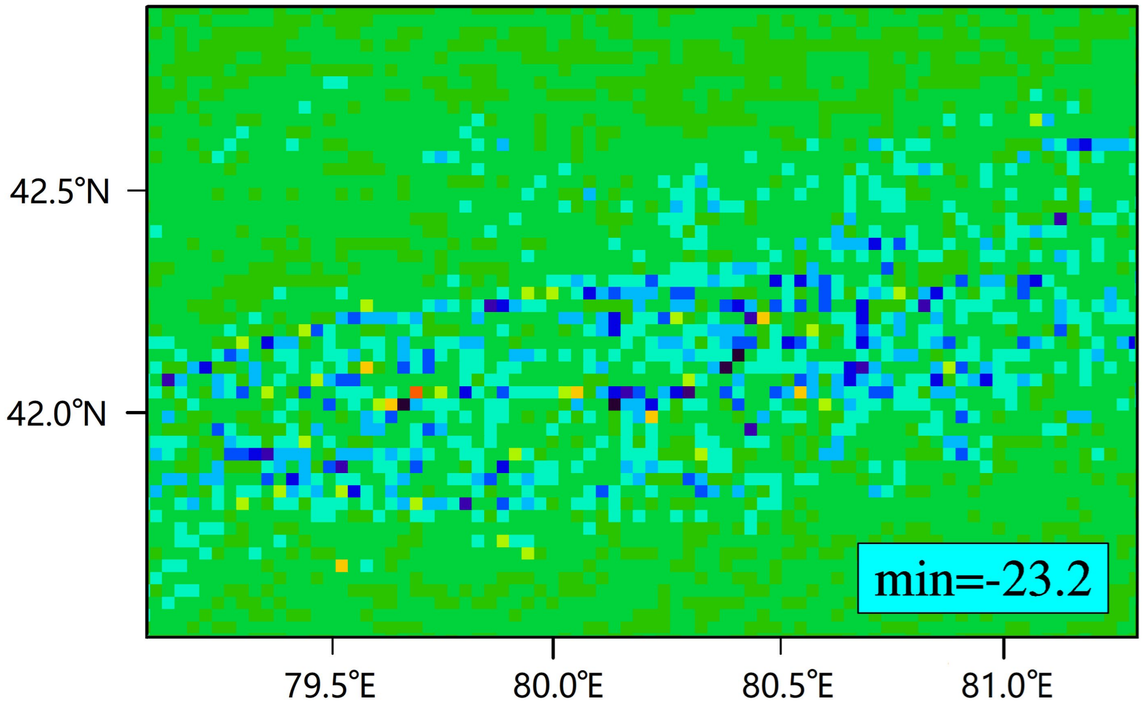

(b) Errors when T_{LK0} = 3.0

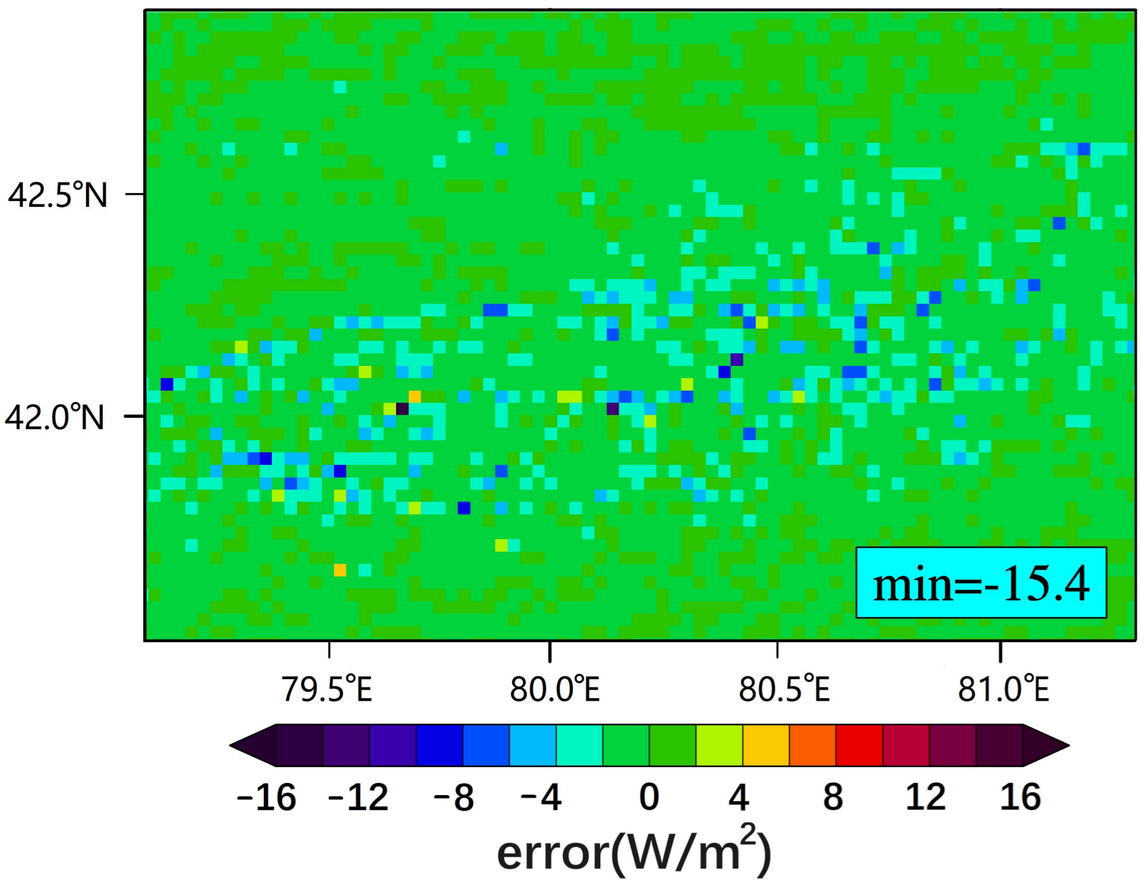

(c) Altitudes of the Tianshan Mountains

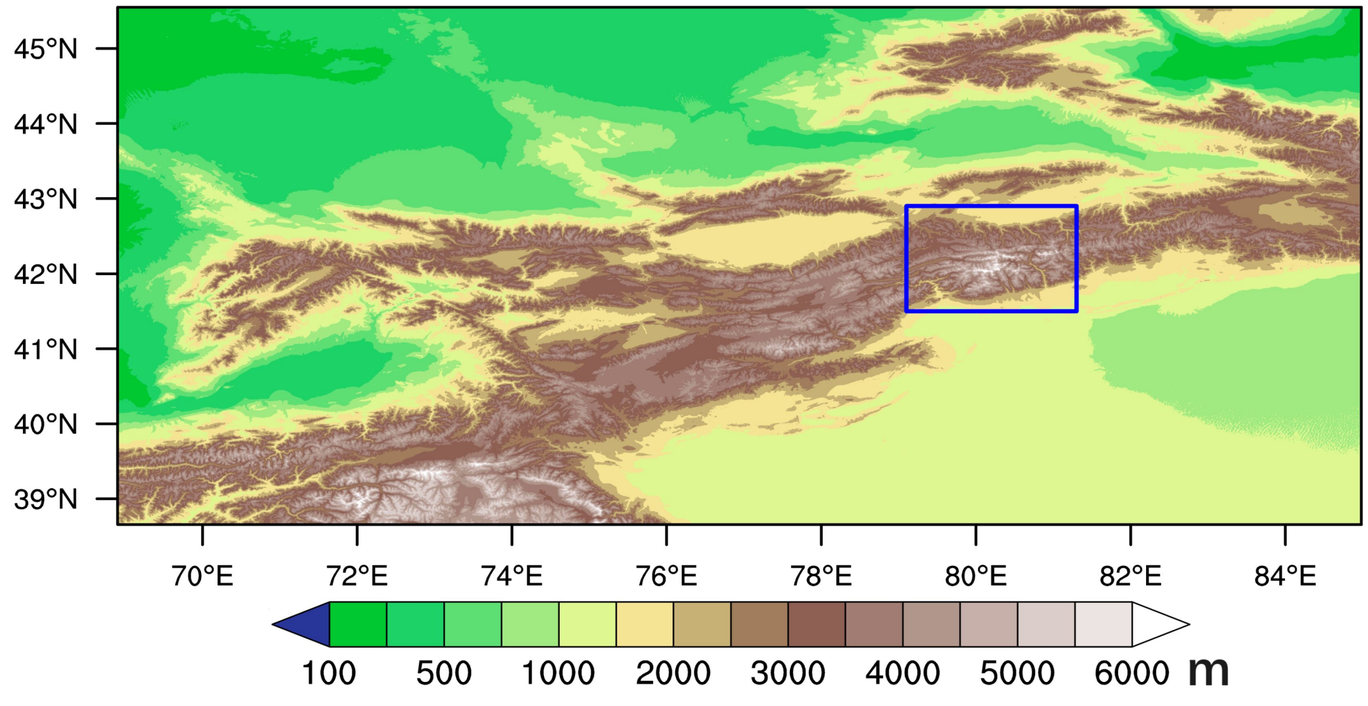

(d) Altitudes in the blue retangle

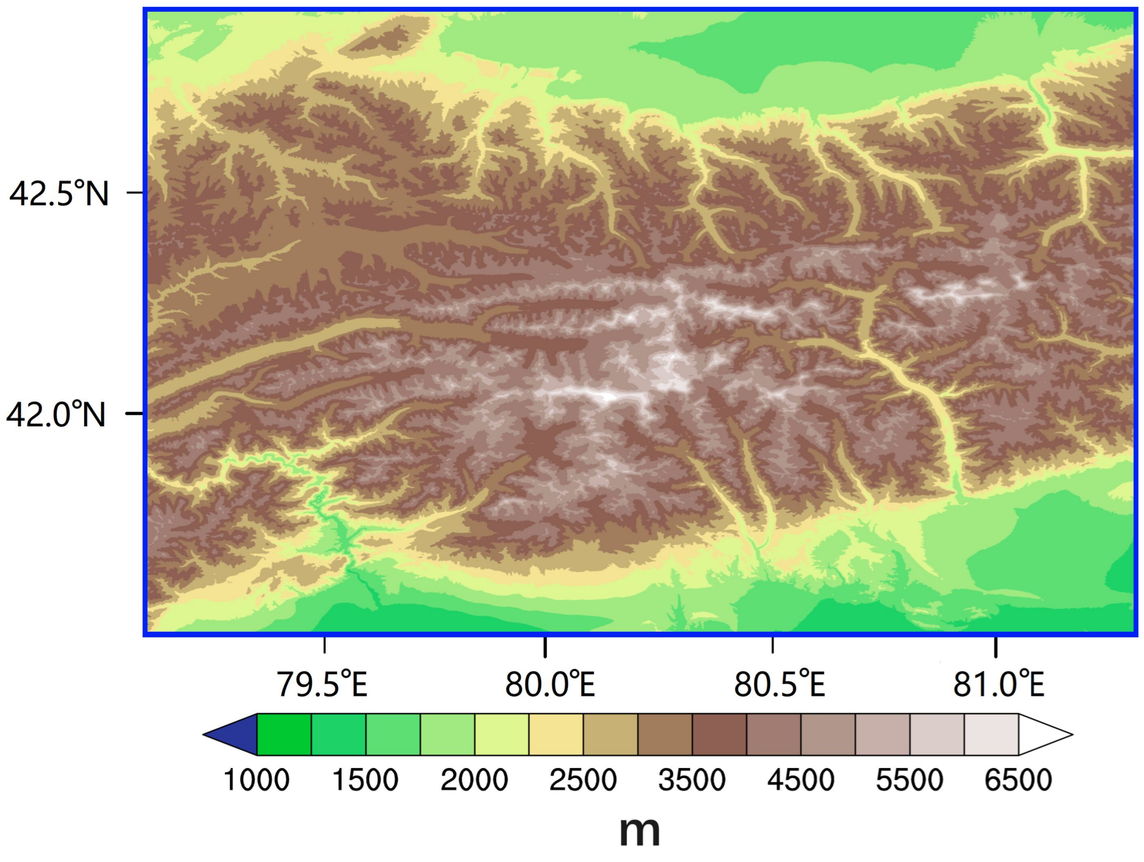

Figure 10.

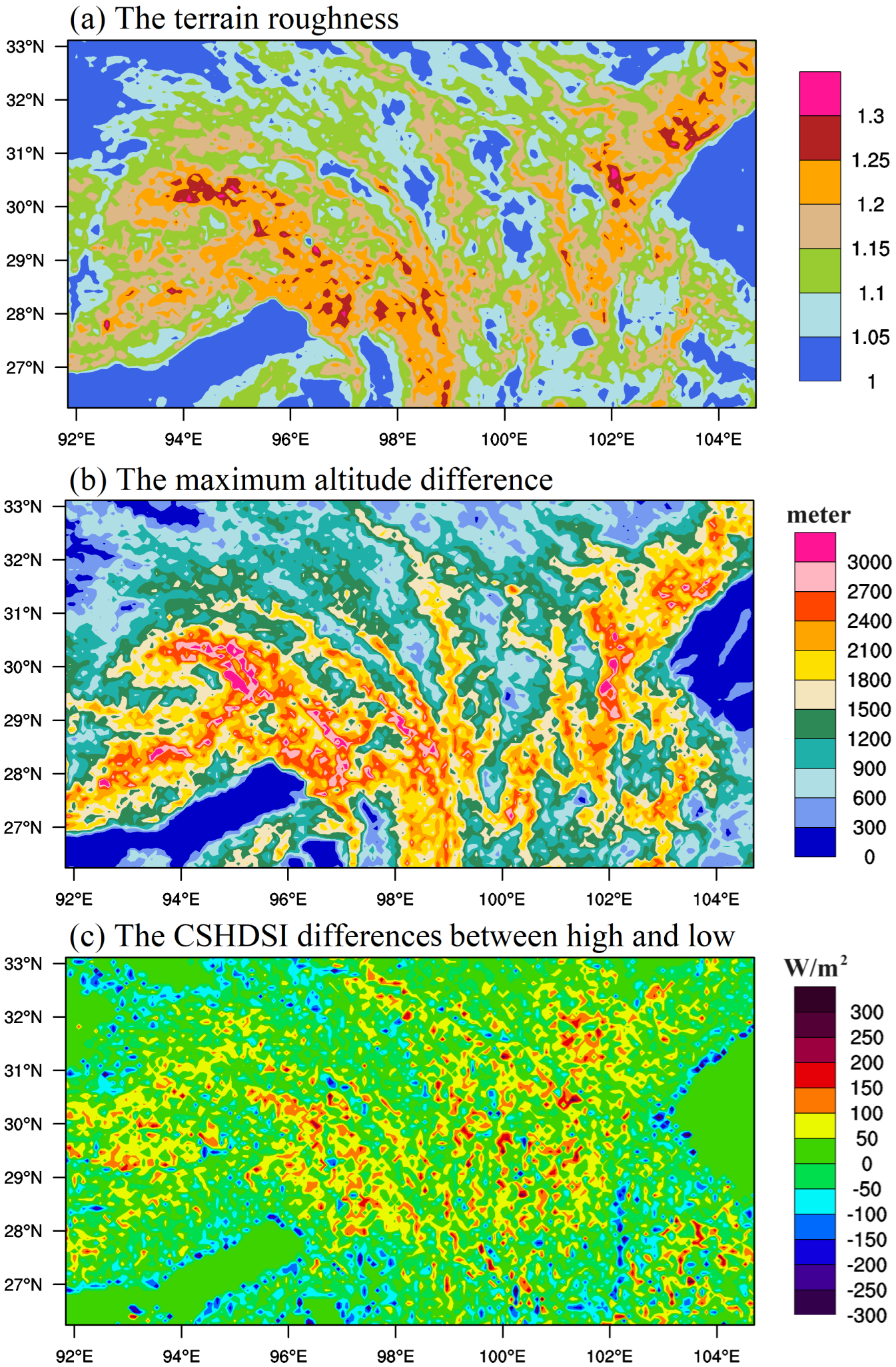
(a) The terrain roughness
33°N
32°N
31°N
30°N
29°N
28°N
27°N
92°E
94°E
96°E
98°E
100°E
102°E
104°E
1.3
1.25
1.2
1.15
1.1
1.05
1
(b) The maximum altitude difference
meter
3000
2700
2400
2100
1800
1500
1200
900
600
300
0
(c) The CSHDSI differences between high and low
W/m²
300
250
200
150
100
50
0
-50
-100
-150
-200
-250
-300